

A positivity preserving strategy for entropy stable discontinuous Galerkin discretizations of the compressible Euler and Navier-Stokes equations

Yimin Lin^a, Jesse Chan^a, Ignacio Tomas^b

^a*Department of Computational and Applied Mathematics, Rice University, 6100 Main St, Houston, TX, 77005*

^b*Sandia National Laboratories¹², P.O. Box 5800, MS 1320, Albuquerque, NM 87185-1320*

Abstract

High-order entropy-stable discontinuous Galerkin methods for the compressible Euler and Navier-Stokes equations require the positivity of thermodynamic quantities in order to guarantee their well-posedness. In this work, we introduce a positivity limiting strategy for entropy-stable discontinuous Galerkin discretizations based on convex limiting. The key ingredient in the limiting procedure is a low order positivity-preserving discretization based on graph viscosity terms. The proposed limiting strategy is both positivity preserving and discretely entropy-stable for the compressible Euler and Navier-Stokes equations. Numerical experiments confirm the high order accuracy and robustness of the proposed strategy.

1. Introduction

Computational fluid dynamics simulations increasingly requires higher resolutions for a variety of applications [1]. High order numerical methods are more accurate per degree of freedom compared to low order methods for sufficiently smooth solutions, so they are more efficient in engineering simulations that require high accuracy [2]. In particular, high-order discontinuous Galerkin (DG) methods are suitable for convection dominated problems, and they can achieve high efficiency due to the locality of most operations [3]. However, high-order DG methods typically suffer from stability issues in the presence of discontinuous solutions, due to the lack of numerical dissipation. High-order entropy stable DG (ESDG) discretizations are high order accurate and satisfy entropy balances at the discrete level for the compressible Euler and Navier-Stokes equations, so they remain robust even on the absence of the chain rule and exact integration at the discrete level [4, 5, 6, 7, 8, 9, 10]. However, a discrete entropy balance is not sufficient to guarantee the stability of high order ESDG schemes. Negative densities and pressure can appear even for smooth solutions [11]. However, entropy-stable schemes assume the positivity of thermodynamic quantities, and such discretizations lose all theoretical stability properties without positivity.

The issue of positivity is intrinsic to the high order polynomial basis, and additional stabilization techniques like artificial viscosity, flux-limiting, slope-limiting, and filtering are typically applied to high-order methods to improve robustness [12, 13, 3]. For DG schemes, Zhang, Shu, and colleagues introduce simple positivity-preserving scaling limiters in [14, 15] using the slope-limiting approach. This limiter can be combined with a local Lax-Friedrichs type positivity-preserving flux for the compressible Euler and Navier-Stokes equations [16, 17].

Another limiting strategy introduced by Kuzmin and colleagues is the algebraic flux-correction strategy [18]. This was generalized by Guermond, Popov, and colleagues using a low-order discretization based on an artificial “graph viscosity” term. The inclusion of this graph viscosity enforces an invariant domain property

¹Sandia National Laboratories is a multimission laboratory managed and operated by National Technology & Engineering Solutions of Sandia, LLC, a wholly-owned subsidiary of Honeywell International Inc., for the U.S. Department of Energy’s National Nuclear Security Administration under contract DE-NA0003525. This document describes objective technical results and analysis. Any subjective views or opinions that might be expressed in the paper do not necessarily represent the views of the U.S. Department of Energy or the United States Government

²SAND No: SAND2022-0960 O

[19, 20, 21, 22]. When combined with the convex-limiting framework (a generalization of the algebraic flux correction framework), this low order discretization can be used to construct limited solutions which are second-order accurate and invariant domain preserving (which implies positivity).

Other strategies include limiters based on sub-cell finite volume schemes [23, 24, 25]. Rueda-Ramirez and Gassner proposed a subcell positivity limiting strategy by blending high-order entropy stable DG discretizations and subcell finite volume discretizations based on Legendre-Gauss-Lobatto (LGL) nodes [26, 27]. Upperman and Yamaleev introduced another positivity preserving strategy by adding artificial dissipation inspired by Brenner-Navier-Stokes diffusion operators [28].

In this work, we develop a positivity preserving strategy for entropy stable DG discretizations using the algebraic flux correction strategy. We first construct a low order positivity preserving scheme for the compressible Euler and Navier-Stokes equations by adding a graph viscosity term. We then define the graph viscosity coefficient using Zhang’s condition on Lax-Friedrichs type dissipation to preserve positivity. We also construct and utilize sparse summation-by-parts (SBP) operators to avoid over-dissipation of the underlying low-order scheme [29]. The limited solution is then obtained by combining the positivity preserving low-order method with the ESDG discretizations via a convex-limiting procedure. The resulting limited solution is conservative and satisfies a semi-discrete entropy balance. We propose two limiting strategies based on the convex-limiting technique and a limiting strategy based on the DG positivity-preserving limiter. Various numerical experiments showcase the robustness of the proposed strategies and demonstrate the difference between each strategy.

The outline of the paper is as follows: Section 2 reviews the compressible Euler and Navier-Stokes equations and the notations used in the paper. Section 3 presents the discrete operators in our proposed discretizations, and Section reviews the high order nodal discontinuous Galerkin discretization. In Section 5 and 6, we introduce the low order positivity preserving discretizations based on graph viscosity and the time discretization. In Section 7 we present the convex limiting technique and an elementwise limiting strategy, and we proved the limited solution is both positivity preserving and satisfies a discrete entropy balance. In Section 8, we provide various numerical experiments in 1D and 2D to verify the convergence and robustness of the proposed limiting strategy. Finally we summarize our work in Section 9.

2. Background knowledge

In this work, we focus on the compressible Euler and Navier-Stokes equations in two space-dimensions. The theoretical contributions of this paper are straightforward to extend to three dimensions.

2.1. Governing equations

The two-dimensional compressible Navier-Stokes equations in conservative form are given by:

$$\frac{\partial \mathbf{u}}{\partial t} + \sum_{i=1}^2 \frac{\partial \mathbf{f}_i^I}{\partial x_i} = \sum_{i=1}^2 \frac{\partial \mathbf{f}_i^V}{\partial x_i}, \quad (1)$$

where \mathbf{u} , \mathbf{f}_i^I , \mathbf{f}_i^V denote the vector of conservative variables, inviscid fluxes, and viscous fluxes respectively.

We follow [30] and write the nondimensional compressible Navier-Stokes equation in 2D as:

$$\frac{\partial}{\partial t} \begin{bmatrix} \rho \\ \rho u \\ \rho v \\ E \end{bmatrix} + \frac{\partial}{\partial x} \begin{bmatrix} \rho u \\ \rho u^2 + p \\ \rho uv \\ (E + p)u \end{bmatrix} + \frac{\partial}{\partial y} \begin{bmatrix} \rho v \\ \rho vu \\ \rho v^2 + p \\ (E + p)v \end{bmatrix} = \frac{1}{\text{Re}} \frac{\partial}{\partial x} \begin{bmatrix} 0 \\ \tau_{xx} \\ \tau_{yx} \\ \tau_{xx}u + \tau_{yx}v + \kappa \frac{\partial T}{\partial x} \end{bmatrix} + \frac{1}{\text{Re}} \frac{\partial}{\partial y} \begin{bmatrix} 0 \\ \tau_{xy} \\ \tau_{yy} \\ \tau_{xy}u + \tau_{yy}v + \kappa \frac{\partial T}{\partial y} \end{bmatrix} \quad (2)$$

Here, ρ, u, v, E denote the density, velocity in the x, y directions, and total mechanical energy respectively. In this work, we assume an ideal gas closure, such that the pressure p and the temperature T are given by the equations of state:

$$p = (\gamma - 1) \rho e, \quad e = c_v T,$$

where e is the specific internal energy, and c_v, γ, κ, μ are specific heat capacity, ratio of specific heats, heat conductivity, and dynamic viscosity respectively. Re , the Reynolds number, and Pr , the Prandtl number, are dimensionless quantities. The relation between the total energy and the specific internal energy is given by:

$$E = \rho e + \frac{1}{2} \rho (u^2 + v^2)$$

The nondimensional compressible Navier-Stokes equations are equivalent to the conservative form (1) through a scaling of physical parameters [30]. In this work, we assume all parameters to refer to their nondimensionalized quantities. The compressible Euler equations are a special case of the compressible Navier-Stokes equations with $\text{Re} \rightarrow \infty$. In other words, the compressible Euler equations describe compressible fluids with zero viscosity and thermal conductivity.

The admissible set of the compressible Euler and Navier-Stokes equations is the set of conservative variables with positive density and specific internal energy. We can write this admissible set as the intersection of superlevel sets of concave functions:

$$\mathcal{A} := \{\mathbf{u} = (\rho, \rho u, E) \mid \rho(\mathbf{u}) > 0, \rho e(\mathbf{u}) > 0\} = \bigcap_{\rho_0 > 0, e_0 > 0} \{\mathbf{u} \mid \rho(\mathbf{u}) \geq \rho_0\} \cap \{\mathbf{u} \mid \rho e(\mathbf{u}) \geq \rho_0 e_0\}. \quad (3)$$

Any physically meaningful solutions to (1) lie in this admissible set, which is a convex set for both sets of equations [16]. The focus of this work is to limit discretely entropy-stable discontinuous Galerkin methods so that the limited solution at each time step remains in \mathcal{A} .

2.2. Entropy variables and the symmetrization of viscous fluxes

Both compressible Euler and Navier-Stokes equations admit a mathematical entropy balance with respect to a convex scalar mathematical entropy

$$\eta(\mathbf{u}) = -\frac{\rho s}{\gamma - 1}$$

where $s = \log\left(\frac{p}{\rho^\gamma}\right)$ denotes the physical entropy [31]. Entropy variables are then defined as the derivative of the mathematical entropy with respect to the conservative variables. The mappings between the entropy variables \mathbf{v} and the conservative variables \mathbf{u} are given by

$$\begin{aligned} \mathbf{v}(\mathbf{u}) &= [v_1 \quad v_2 \quad v_3 \quad v_4] = \begin{bmatrix} \frac{\rho e(\gamma+1-s)-E}{\rho e} & \frac{u}{e} & \frac{v}{e} & -\frac{1}{e} \end{bmatrix} \\ \mathbf{u}(\mathbf{v}) &= [-(\rho e)v_4 \quad \rho e v_2 \quad \rho e v_3 \quad \rho e \left(1 - \frac{v_2^2 + v_3^2}{2v_4}\right)]. \end{aligned}$$

Internal energy and physical entropy can be written in terms of entropy variables

$$\rho e = \left(\frac{\gamma - 1}{(-v_4)^\gamma}\right)^{1/(\gamma-1)} e^{-\frac{s}{\gamma-1}}, \quad s = \gamma - v_1 + \frac{v_2^2 + v_3^2}{2v_4}.$$

The entropy variables symmetrize the viscous fluxes in the following sense

$$\frac{\partial \mathbf{f}_1^V}{\partial x} + \frac{\partial \mathbf{f}_2^V}{\partial y} = \nabla \cdot (\mathbf{K} \nabla \mathbf{v}) = \frac{\partial}{\partial x} \left(\mathbf{K}_{11} \frac{\partial \mathbf{v}}{\partial x} + \mathbf{K}_{12} \frac{\partial \mathbf{v}}{\partial y} \right) + \frac{\partial}{\partial y} \left(\mathbf{K}_{21} \frac{\partial \mathbf{v}}{\partial x} + \mathbf{K}_{22} \frac{\partial \mathbf{v}}{\partial y} \right), \quad (4)$$

where \mathbf{K}_{ij} are blocks of a symmetric positive definite matrix \mathbf{K}

$$\mathbf{K} = \begin{bmatrix} \mathbf{K}_{11} & \mathbf{K}_{12} \\ \mathbf{K}_{21} & \mathbf{K}_{22} \end{bmatrix}$$

2.3. On notation

We follow the notation convention introduced in [6]. Vector and matrix quantities are denoted using lower and upper case bold fonts respectively, for example, \mathbf{A} and \mathbf{u} . Spatially discrete quantities are written in bold sans serif font, for example, \mathbf{x} . For clarity, continuous real functions evaluated over spatially discrete quantities are taken to mean point-wise evaluations. For example,

$$\mathbf{x} = \begin{bmatrix} \mathbf{x}_1 \\ \vdots \\ \mathbf{x}_n \end{bmatrix}, \quad u : \mathbb{R} \rightarrow \mathbb{R}, \quad u(\mathbf{x}) = \begin{bmatrix} u(\mathbf{x}_1) \\ \vdots \\ u(\mathbf{x}_n) \end{bmatrix}$$

The L^2 inner products over an element D and the boundary of element ∂D is denoted by

$$(\mathbf{u}, \mathbf{v})_D = \int_D \mathbf{u} \cdot \mathbf{v} \, d\mathbf{x}, \quad \langle \mathbf{u}, \mathbf{v} \rangle_{\partial D} = \int_{\partial D} \mathbf{u} \cdot \mathbf{v} \, d\mathbf{x}.$$

For systems of conservation laws, there are multiple scalar components. When $\mathbf{A} \in \mathbb{R}^{m \times m}$, $\mathbf{u} \in \mathbb{R}^{mn}$, we will regard $\mathbf{A}\mathbf{u}$ as the Kronecker product $(\mathbf{A} \otimes \mathbf{I}_n)\mathbf{u}$.

In this paper, we will adopt the lexicographical ordering of nodes and basis functions, so that a multi-index is replaced by a lexicographical single index for clarity of notation. We discretize time derivatives with forward Euler time discretizations for brevity. The extension to higher-order time discretizations is straightforward and will be discussed in Section 7. We will use a number subscript $\mathbf{A}_1, \mathbf{A}_2$ or a letter subscript $\mathbf{A}_r, \mathbf{A}_s$ interchangeably to indicate the coordinates of discrete operators. This work will present the theory on the reference element \hat{D} and ignore the involving geometric terms for clarity of notation. We refer readers to [32, 33] for the extension of high order ESDG schemes to curved meshes. The extension of positivity preserving schemes via convex-limiting to curved meshes follows is detailed in [29].

3. Discrete operators

We denote the computational domain by $\Omega \subseteq \mathbb{R}^2$. We discretize the domain by non-overlapping tensor product or simplicial elements D^k . We assume physical elements are the images of the reference element \hat{D} through an affine mapping $\Phi^k(\mathbf{r}, \mathbf{s})$. Affine transformation implies that Jacobian determinants are constant on each element. The extension to curvilinear meshes can be found in [32].

3.1. Multidimensional Summation-By-Parts operators

The construction of the numerical scheme in this work relies on the summation-by-parts (SBP) operators [34]. In this work, we focus on diagonal-norm SBP operators, which are differentiation matrices weighted by diagonal mass matrices. An SBP quadrature rule (\mathbf{r}, \mathbf{w}) induces the SBP operators. A SBP quadrature rule is a volume quadrature rule that contains identically distributed boundary points on each face that forms a separate surface quadrature rule $(\mathbf{r}^f, \mathbf{w}^f)$. We require the quadrature weights to be positive, and the volume and surface quadrature rules are exact for polynomials of degree $2N - 1$ and $2N$ respectively.

Figure 1 illustrates the SBP quadrature points on a tensor product and a simplicial reference element. The SBP quadrature on tensor product elements is the tensor product of the Gauss-Lobatto quadrature, and the surface quadrature rule on simplicial elements is the Gauss-Lobatto quadrature. We denote the number of collocated nodes by N_p and the number of surface quadrature points by N_p^f .

We can then define the lumped mass matrix using SBP quadrature weights:

$$\mathbf{M} = \begin{bmatrix} \mathbf{w}_1 & & & \\ & \ddots & & \\ & & \ddots & \\ & & & \mathbf{w}_{N_p} \end{bmatrix},$$

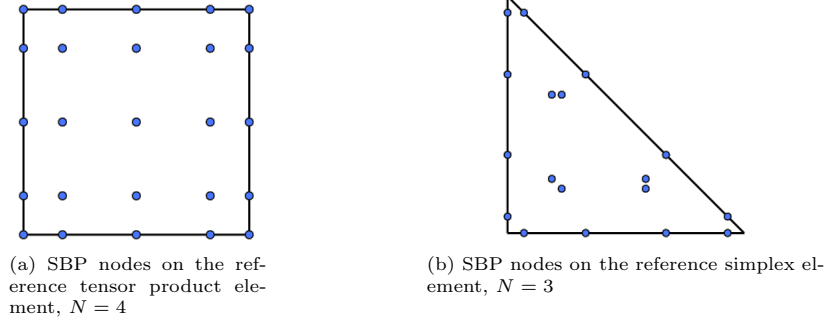


Figure 1: SBP quadrature rules

and we denote the nodal differentiation matrices by:

$$(\mathbf{D}_r \mathbf{u})_i = \frac{\partial \mathbf{u}}{\partial r} \Big|_{r=r_i}, \quad (\mathbf{D}_s \mathbf{u})_i = \frac{\partial \mathbf{u}}{\partial s} \Big|_{s=s_i},$$

where \mathbf{u} is the nodal values at quadrature points. We define \mathbf{E} as the extrapolation (or face extraction) matrix from the volume quadrature points to the surface quadrature points. Since we assume the SBP quadrature includes the surface quadrature points, the extrapolation matrix is a matrix of size $N_p^f \times N_p$ with entries either 0 or 1. The boundary integration matrices of size $N_p^f \times N_p^f$ are defined as,

$$\mathbf{B}_r = \begin{bmatrix} \mathbf{w}_1^f \hat{\mathbf{n}}_{r,1} & & \\ & \ddots & \\ & & \mathbf{w}_{N_p^f}^f \hat{\mathbf{n}}_{r,N_p^f} \end{bmatrix}, \quad \mathbf{B}_s = \begin{bmatrix} \mathbf{w}_1^f \hat{\mathbf{n}}_{s,1} & & \\ & \ddots & \\ & & \mathbf{w}_{N_p^f}^f \hat{\mathbf{n}}_{s,N_p^f} \end{bmatrix},$$

where $\hat{\mathbf{n}}_r, \hat{\mathbf{n}}_s$ are components of outward normal vectors of the reference element.

We introduce the SBP operators \mathbf{Q} (e.g. the differentiation matrices weighted by the lumped mass matrix), which satisfy the SBP property:

$$\mathbf{Q}_r + \mathbf{Q}_r^T = \mathbf{E}^T \mathbf{B}_r \mathbf{E}, \quad \mathbf{Q}_s + \mathbf{Q}_s^T = \mathbf{E}^T \mathbf{B}_s \mathbf{E}. \quad (5)$$

The SBP property replicates integration by parts at a discrete level in the following way:

$$\mathbf{u}^T (\mathbf{Q}_r + \mathbf{Q}_r^T) \mathbf{v} = \mathbf{u}^T \mathbf{E}^T \mathbf{B}_r \mathbf{E} \mathbf{v} \iff \left(\mathbf{u}, \frac{\partial \mathbf{v}}{\partial r} \right)_{\hat{D}} + \left(\frac{\partial \mathbf{u}}{\partial r}, \mathbf{v} \right)_{\hat{D}} = \langle \mathbf{u}, \mathbf{v} \hat{\mathbf{n}}_r \rangle_{\partial \hat{D}} \quad (6)$$

We can write the SBP operator as the sum of its skew-symmetric part and the boundary integration matrix:

$$\mathbf{Q}_r = \mathbf{M} \mathbf{D}_r = \frac{\mathbf{Q}_r - \mathbf{Q}_r^T}{2} + \frac{1}{2} \mathbf{E}^T \mathbf{B}_r \mathbf{E}, \quad \mathbf{Q}_r \mathbf{1} = 0, \quad (7)$$

$$\mathbf{Q}_s = \mathbf{M} \mathbf{D}_s = \frac{\mathbf{Q}_s - \mathbf{Q}_s^T}{2} + \frac{1}{2} \mathbf{E}^T \mathbf{B}_s \mathbf{E}, \quad \mathbf{Q}_s \mathbf{1} = 0. \quad (8)$$

3.2. Sparse low order Summation-By-Parts operators

Given a set of SBP quadrature points, we can construct sparse low-order summation-by-parts operators \mathbf{Q}^L . Since we will construct a low-order scheme by applying an algebraic dissipation operator based on the sparsity pattern of our discrete operators, we seek operators which are sparse to avoid introducing

unnecessary dissipation in the low-order algebraic scheme [29]. We require only that the operators satisfy an SBP property and a conservation property:

$$\mathbf{Q}_r^L + \left(\mathbf{Q}_r^L\right)^T = \mathbf{E}^T \mathbf{B}_r \mathbf{E}, \quad \mathbf{Q}_r^L \mathbf{1} = 0, \quad (9)$$

$$\mathbf{Q}_s^L + \left(\mathbf{Q}_s^L\right)^T = \mathbf{E}^T \mathbf{B}_s \mathbf{E}, \quad \mathbf{Q}_s^L \mathbf{1} = 0. \quad (10)$$

For tensor product elements, we follow [29] and construct sparse low order SBP operators are derived by integrating the piecewise linear basis \mathbf{p}_i constructed on the LGL nodes

$$\left(\mathbf{Q}_{1D}^L\right)_{ij} = \int_{\hat{D}} \mathbf{p}_i \frac{\partial \mathbf{p}_j}{\partial r} dr, \quad \mathbf{Q}_{1D}^L = \begin{bmatrix} -\frac{1}{2} & \frac{1}{2} & & \\ -\frac{1}{2} & 0 & \frac{1}{2} & \\ & -\frac{1}{2} & 0 & \frac{1}{2} \\ & & & \ddots \end{bmatrix}, \quad \mathbf{Q}_r^L = \mathbf{I}_{N_P} \otimes \mathbf{Q}_{1D}^L, \quad \mathbf{Q}_s^L = \mathbf{Q}_{1D}^L \otimes \mathbf{I}_{N_P}$$

For simplicial elements, we follow [35] and build a sparse operators based on a stencil (or a connectivity graph) built from the SBP quadrature points. Then, we restrict the low order SBP operator to have the same sparsity pattern as the adjacency matrix of the graph. In particular, we define the adjacency matrix \mathbf{A} and the graph Laplacian \mathbf{L} as:

$$(\mathbf{A})_{ij} = \begin{cases} 1 & \text{if } \|\mathbf{r}_i - \mathbf{r}_j\|_2 \leq \alpha \max \left\{ \left(\frac{\mathbf{w}_i}{\pi}\right)^\beta, \left(\frac{\mathbf{w}_j}{\pi}\right)^\beta \right\} \\ 0 & \text{otherwise} \end{cases}, \quad (\mathbf{L})_{ij} = \begin{cases} \deg(\mathbf{r}_i) & \text{if } i = j \\ -1 & \text{if } \mathbf{A}_{ij} \neq 0 \\ 0 & \text{otherwise} \end{cases}, \quad (11)$$

where $\alpha, \beta \in \mathbb{R}$ are parameters. In particular, when $\alpha = 1, \beta = \frac{1}{2}$, two quadrature points are considered “adjacent” if they both lie in the circle of area $\max \{\mathbf{w}_i, \mathbf{w}_j\}$ centered at either quadrature point. In one-space dimension this is equivalent to the notion of “three-point stencil”: for each time step, the evolution of the solution at the current node depends only on its own value and the value of its immediate neighbors.

Then, we can define the sparse low order SBP operator by making the ansatz $\frac{1}{2}(\mathbf{Q} - \mathbf{Q}^T)_{ij} = \psi_j - \psi_i$ [36] and solving the constrained linear system:

$$\begin{aligned} \mathbf{Q}_r^L \mathbf{1} &= 0 \\ \text{s.t.} \quad \left(\frac{\mathbf{Q}_r^L - \left(\mathbf{Q}_r^L\right)^T}{2} \right)_{ij} &= \begin{cases} 0 & \text{if } \mathbf{L}_{ij} = 0 \\ \psi_j - \psi_i & \text{otherwise} \end{cases} \\ \mathbf{Q}_r^L &= \frac{\mathbf{Q}_r^L - \left(\mathbf{Q}_r^L\right)^T}{2} + \frac{1}{2} \mathbf{E}^T \mathbf{B} \mathbf{E} \\ \psi^T \mathbf{1} &= 0, \end{aligned}$$

which reduces to

$$\mathbf{L} \psi = \frac{1}{2} \mathbf{E}^T \mathbf{B} \mathbf{E} \mathbf{1} \quad \text{s.t.} \quad \psi^T \mathbf{1} = 0.$$

The constraint $\psi^T \mathbf{1} = 0$ ensures the existence and uniqueness of the solution. We refer interested readers to [35] for a more detailed description of this process.

4. High order entropy-stable discontinuous Galerkin discretizations

In this section, we will review the nodal entropy stable DG methods for the compressible Euler and Navier-Stokes equations. Entropy conservative numerical fluxes as introduced by Tadmor [37, 38] are fundamental to construct entropy stable DG schemes. They are symmetric bivariate functions $\mathbf{f}_S(\mathbf{u}_L, \mathbf{u}_R)$ that

are consistent with respect to a given flux $\mathbf{f}(\mathbf{u})$, i.e. $\mathbf{f}_S(\mathbf{u}, \mathbf{u}) = \mathbf{f}(\mathbf{u})$. In addition, they satisfy an entropy conservation property $(\mathbf{v}_L - \mathbf{v}_R)^T \mathbf{f}_S(\mathbf{u}_L, \mathbf{u}_R) = \psi(\mathbf{u}_L) - \psi(\mathbf{u}_R)$, which relates the entropy variables and entropy potential $\psi(\mathbf{u})$ at a discrete level. There exist entropy-conservative numerical fluxes with respect to the inviscid flux $f_i^I(\mathbf{u})$ for the compressible Euler and Navier-Stokes equations. For example, Chandrashekar derived an entropy conservative and kinetic energy preserving numerical flux [39] that satisfies the above properties.

The derivative of the inviscid flux f_i^I can then be reformulated using the entropy conservative flux. The reformulation is commonly referred to as “flux differencing” and can be interpreted as a high-order subcell-based finite volume formulation. Gassner, Winter, and Kopriva provide a continuous interpretation of the technique [40, 4]

$$\frac{\partial f_i^I(\mathbf{u}(\mathbf{x}))}{\partial x_i} = 2 \frac{\partial f_{i,S}(\mathbf{u}(\mathbf{x}), \mathbf{u}(\mathbf{y}))}{\partial x_i} \Big|_{\mathbf{y}=\mathbf{x}}$$

Then, we can discretize the variational form of the derivative of the inviscid flux using the high order weighted differentiation matrix and the the row sum of a Hadamard product

$$\int_{\hat{D}} \frac{\partial f_k^I(\mathbf{u})}{\partial x_k} \vec{\mathbf{l}} \xrightarrow{\text{Discretize}} 2(\mathbf{Q}_k \circ \mathbf{F}_k) \mathbf{1}, \quad (\mathbf{F}_k)_{ij} = f_{k,S}(\mathbf{u}_i, \mathbf{u}_j), \quad (12)$$

where $\vec{\mathbf{l}}$ denotes the vector of Lagrange interpolation polynomials.

The entropy conservative DG formulation in a variational strong form for the compressible Euler equation can then be written as follows,

$$\mathbf{M} \frac{\partial \mathbf{u}}{\partial t} + \sum_{k=1}^2 2(\mathbf{Q}_k \circ \mathbf{F}_k) \mathbf{1} + \sum_{k=1}^2 \mathbf{E}^T \mathbf{B}_k (\mathbf{f}_k^{I,*} - \mathbf{f}_k^I) = 0 \quad (13)$$

We can rewrite the formulation in the skew-symmetric form by using the SBP property of the weighted differentiation matrix,

$$\mathbf{M} \frac{\partial \mathbf{u}}{\partial t} + \sum_{k=1}^2 \left((\mathbf{Q}_k - \mathbf{Q}_k^T) \circ \mathbf{F}_k \right) \mathbf{1} + \sum_{k=1}^2 \mathbf{E}^T \mathbf{B}_k \mathbf{f}_k^{I,*} = 0 \quad (14)$$

where we denote the interface numerical flux by $\mathbf{f}_k^{I,*}$. This will be specified later in Section 6.2.

To discretize the derivative of symmetrized viscous fluxes, we first rewrite the viscous term as a first-order system of partial differential equations through the derivative of entropy variables and auxiliary variables. Then we can derive an LDG-type formulation for the first-order system [6],

$$\begin{aligned} \Theta_i &= \frac{\partial v}{\partial x_i} & \mathbf{M} \Theta_i &= \frac{\mathbf{Q}_i - \mathbf{Q}_i^T}{2} \mathbf{v} + \mathbf{E}^T \mathbf{B}_i \mathbf{v}^* \\ \sigma_i &= \mathbf{K}_{i1} \Theta_1 + \mathbf{K}_{i2} \Theta_2 & \xrightarrow{\text{Discretize}} \sigma_i &= \mathbf{K}_{i1} \Theta_1 + \mathbf{K}_{i2} \Theta_2 \\ \frac{\partial \mathbf{f}_1^V}{\partial x_1} + \frac{\partial \mathbf{f}_2^V}{\partial x_2} &= \frac{\partial \sigma_1}{\partial x_1} + \frac{\partial \sigma_2}{\partial x_2} & \mathbf{M} \mathbf{H} &= \sum_{k=1}^2 \left((\mathbf{Q}_k - \mathbf{Q}_k^T) \circ \mathbf{F}_k^\sigma \right) \mathbf{1} + \sum_{k=1}^2 \mathbf{E}^T \mathbf{B}_k \sigma_k^* \\ & & (\mathbf{F}_k^\sigma)_{ij} &= \frac{(\sigma_k)_i + (\sigma_k)_j}{2}, \\ & & (\mathbf{v}^*)_i &= \frac{v_i + v_i^+}{2}, \quad (\sigma_k^*)_i = \frac{(\sigma_k)_i + (\sigma_k)_i^+}{2}, \end{aligned} \quad (15)$$

where $\mathbf{M} \mathbf{H}$ is the discretization of $\int_{\hat{D}} \left(\frac{\partial \sigma_1}{\partial x_1} + \frac{\partial \sigma_2}{\partial x_2} \right) \vec{\mathbf{l}}$. Here we write the product of the SBP operator and the flux vector as the Hadamard product between the SBP operator and a central flux matrix [6]. This formulation will become useful in future sections.

Under appropriate choices of interface flux and interface penalization, formulations (13), (14) and (15) satisfy semi-discrete entropy balances. For details of the proof, readers may refer to [6]. For completeness, we state the semi-discrete entropy balance for the compressible Navier-Stokes equation for reference:

Theorem 4.1. Assume continuity in time and positivity of the density and internal energy. If the domain is periodic, then

$$\frac{d}{dt} \int_{\Omega} \eta(\mathbf{u}) \approx \mathbf{1}^T \mathbf{W} \frac{d\eta(\mathbf{u})}{dt} = \mathbf{v}^T \mathbf{M} \frac{\partial \mathbf{u}}{\partial t} \leq - \sum_{i,j=1}^2 \Theta_i^T \mathbf{M} \mathbf{K}_{ij} \Theta_j \leq 0,$$

which corresponds to the continuous entropy balance

$$\int_{\Omega} \frac{\partial \eta(\mathbf{u})}{\partial t} = \int_{\Omega} \left(\frac{\partial \mathbf{u}}{\partial t} \right)^T \mathbf{v}(\mathbf{u}) \leq \int_{\Omega} \sum_{i,j=1}^2 \left(\frac{\partial \mathbf{v}}{\partial x_i} \right)^T \left(\mathbf{K}_{ij} \frac{\partial \mathbf{v}}{\partial x_j} \right)$$

This discrete entropy balance extends also to certain non-periodic boundary conditions (for example, adiabatic or reflective walls) [6].

5. A positivity preserving method for the compressible Euler and Navier-Stokes equations

Nonlinear stability holds only when density and internal energy are positive. However, one cannot a-priori guarantee the positivity of the solution. In this section, we will introduce a sparse low-order positivity preserving discretizations. The formulation is based on a sparse low order DG discretization, and with the addition of an artificial dissipation term (usually referred to as graph viscosity [20]), the schemes will achieve the desired positivity preserving property.

The sparse low-order positivity preserving DG discretization can be written in matrix form as

$$\begin{aligned} \mathbf{M} \frac{\partial \mathbf{u}}{\partial t} + \sum_{k=1}^2 \left(\left(\mathbf{Q}_k^L - \left(\mathbf{Q}_k^L \right)^T \right) \circ \mathbf{F}_k \right) \mathbf{1} - (\mathbf{\Lambda} \circ \mathbf{D}) \mathbf{1} + \sum_{k=1}^2 \mathbf{E}^T [\mathbf{B}_k \mathbf{f}_k^* - \lambda_k \llbracket \mathbf{u} \rrbracket] &= 0 \\ (\mathbf{F}_k)_{ij} = \frac{1}{2} \left(\mathbf{f}_{k,i}^I + \mathbf{f}_{k,i}^I - (\sigma_k)_i - (\sigma_k)_j \right), \quad \mathbf{f}_k^* = \frac{1}{2} \left(\mathbf{f}_{k,i}^{I,+} + \mathbf{f}_{k,i}^{I,+} - (\sigma_k)_i - (\sigma_k)_i^+ \right) \\ \mathbf{\Lambda}_{ij} = \lambda_{ij}, \quad (\mathbf{D}_{ij}) = \mathbf{u}_j - \mathbf{u}_i, \end{aligned} \quad (16)$$

where $\sigma = 0$ for the compressible Euler equation in this section for brevity.

Formulation 16 starts from the skew-symmetric form of the discontinuous Galerkin collocation spectral element discretizations [8]. We use the lumped mass matrix \mathbf{M} induced from SBP quadrature to evaluate the integrals at the discrete level. Then, we replace the high-order SBP operators \mathbf{Q}_k with the sparse low-order operators \mathbf{Q}_k^L introduced in Section 3. As suggested in [29], sparsifying the SBP operator prevents the accuracy of the proposed discretization from decreasing as the order of approximation increases [29]. The numerical fluxes at inter-element interfaces are central fluxes.

The key to achieving the positivity preserving property is the addition of the graph viscosity term $(\mathbf{\Lambda} \circ \mathbf{D}) \mathbf{1}$ and the penalization $\lambda_k \llbracket \mathbf{u} \rrbracket$ at interfaces. The viscosity coefficients are chosen as

$$\begin{aligned} \lambda_{ij} &= \max \left(\alpha \left(\mathbf{u}_i, \mathbf{u}_j, \sigma_i, \sigma_j, \frac{\mathbf{n}_{ij}}{\|\mathbf{n}_{ij}\|} \right) \|\mathbf{n}_{ij}\|, \alpha \left(\mathbf{u}_j, \mathbf{u}_i, \sigma_j, \sigma_i, \frac{\mathbf{n}_{ji}}{\|\mathbf{n}_{ji}\|} \right) \|\mathbf{n}_{ji}\| \right), \\ (\lambda_k)_i &= \frac{|\mathbf{B}_k|_{ii}}{2} \alpha \left(\mathbf{u}_i, \mathbf{u}_i^+, \sigma_i, \sigma_i^+, \hat{\mathbf{n}}_i \right), \quad \mathbf{n}_{ij} = \frac{1}{2} \begin{bmatrix} \left(\mathbf{Q}_r^L - \left(\mathbf{Q}_r^L \right)^T \right)_{ij} \\ \left(\mathbf{Q}_s^L - \left(\mathbf{Q}_s^L \right)^T \right)_{ij} \end{bmatrix} \end{aligned} \quad (17)$$

We note that the viscosity coefficient λ_{ij} is nonzero if and only if $\left(\left(\mathbf{Q}_r^L - \left(\mathbf{Q}_r^L \right)^T \right) \right)_{ij}$ or $\left(\left(\mathbf{Q}_s^L - \left(\mathbf{Q}_s^L \right)^T \right) \right)_{ij}$ is nonzero. Equivalently, the graph viscosity term has the same sparsity pattern as the graph-Laplacian \mathbf{L} excluding the diagonal entries.

The viscosity coefficient $\alpha(\mathbf{u}_i, \mathbf{u}_j, \boldsymbol{\sigma}_i, \boldsymbol{\sigma}_j, \frac{\mathbf{n}_{ij}}{\|\mathbf{n}_{ij}\|})$ determines the amount of dissipation applied to ensure positivity. For both sets of equations, we use the coefficients in the local Lax-Friedrichs type positivity-preserving flux introduced in [16]. We define

$$\alpha(\mathbf{u}_L, \mathbf{u}_R, \boldsymbol{\sigma}_L, \boldsymbol{\sigma}_R, \mathbf{n}) = \max\{\beta(\mathbf{u}_L, \boldsymbol{\sigma}_L, \mathbf{n}), \beta(\mathbf{u}_R, \boldsymbol{\sigma}_R, \mathbf{n})\} \quad (18)$$

$$\beta(\mathbf{u}, \boldsymbol{\sigma}, \mathbf{n}) = \epsilon_0 + |\mathbf{n} \cdot \mathbf{u}| + \frac{1}{2\rho^2 e} \left(\sqrt{\rho^2 (\mathbf{q} \cdot \mathbf{n})^2 + 2\rho^2 e \|\mathbf{n} \cdot \boldsymbol{\tau} - p\mathbf{n}\|^2} + \rho |\mathbf{q} \cdot \mathbf{n}| \right), \quad (19)$$

$$\mathbf{n} \cdot \boldsymbol{\tau} = \begin{bmatrix} \mathbf{n}_1 (\boldsymbol{\sigma}_1)_2 + \mathbf{n}_2 (\boldsymbol{\sigma}_1)_3 \\ \mathbf{n}_1 (\boldsymbol{\sigma}_2)_2 + \mathbf{n}_2 (\boldsymbol{\sigma}_2)_3 \end{bmatrix}, \quad \mathbf{q} = \begin{bmatrix} \mathbf{u}_1 (\boldsymbol{\sigma}_1)_2 + \mathbf{u}_2 (\boldsymbol{\sigma}_1)_3 - (\boldsymbol{\sigma}_1)_4 \\ \mathbf{u}_1 (\boldsymbol{\sigma}_2)_2 + \mathbf{u}_2 (\boldsymbol{\sigma}_2)_3 - (\boldsymbol{\sigma}_2)_4 \end{bmatrix}$$

where ϵ_0 is a positive number arbitrarily close to 0. The coefficient β allows the construction of admissible intermediate states. We present the characterization of the admissibility of the artificial intermediate state in terms of discrete variables $\boldsymbol{\sigma}$ as [16]:

$$\beta \mathbf{u} \pm (\mathbf{f}^I(\mathbf{u}) - \boldsymbol{\sigma}) \cdot \mathbf{n} \in \mathcal{A} \iff \beta > |\mathbf{n} \cdot \mathbf{u}| + \frac{1}{2\rho^2 e} \left(\sqrt{\rho^2 (\mathbf{q} \cdot \mathbf{n})^2 + 2\rho^2 e \|\mathbf{n} \cdot \boldsymbol{\tau} - p\mathbf{n}\|^2} + \rho |\mathbf{q} \cdot \mathbf{n}| \right), \quad (20)$$

where \mathbf{n} is any unit normal vector.

We can alternatively interpret the low order scheme (16) as a low order subcell-based finite volume method using local Lax-Friedrichs type fluxes. In particular, an equivalent form of the formulation (16) is

$$\begin{aligned} \mathbf{M} \frac{\partial \mathbf{u}}{\partial t} + 2 \left(\|\mathbf{n}_{ij}\| \circ \widehat{\mathbf{F}} \right) \mathbf{1} + \mathbf{E}^T \mathbf{W}_f \widehat{\mathbf{f}}^* &= 0, \\ \widehat{\mathbf{F}}_{ij} &= \widehat{\mathbf{f}} \left(\mathbf{u}_i, \mathbf{u}_j, \frac{\mathbf{n}_{ij}}{\|\mathbf{n}_{ij}\|} \right), \quad \widehat{\mathbf{f}}_i^* = \widehat{\mathbf{f}}(\mathbf{u}_i, \mathbf{u}_i^+, \widehat{\mathbf{n}}_i), \end{aligned} \quad (21)$$

where $\|\mathbf{n}_{ij}\|$ denotes the matrix whose (i, j) entry is $\|\mathbf{n}_{ij}\|$ defined in (17). We define the local Lax-Friedrichs flux as

$$\widehat{\mathbf{f}}(\mathbf{u}_L, \mathbf{u}_R, \mathbf{n}) = \mathbf{n} \cdot \frac{\mathbf{f}(\mathbf{u}_L) + \mathbf{f}(\mathbf{u}_R)}{2} - \frac{\alpha(\mathbf{u}_L, \mathbf{u}_R, \boldsymbol{\sigma}_L, \boldsymbol{\sigma}_R, \mathbf{n})}{2} (\mathbf{u}_R - \mathbf{u}_L) \quad (22)$$

By the SBP properties (9) and (10), we can rewrite the formulation (16) over each row i as:

$$\begin{aligned} \mathbf{m}_i \frac{\mathbf{u}_i^{L, n+1} - \mathbf{u}_i}{\tau} + \sum_{j \in \mathcal{I}(i)} \sum_{k=1}^2 \left(\mathbf{Q}_k^L - \left(\mathbf{Q}_k^L \right)^T \right)_{ij} \frac{\mathbf{f}_k(\mathbf{u}_j) - \mathbf{f}_k(\mathbf{u}_i)}{2} - \lambda_{ij} (\mathbf{u}_j + \mathbf{u}_i) \\ + \sum_{j \in \mathcal{B}(i)} \sum_{k=1}^2 \left(\mathbf{E}^T \mathbf{B}_k \mathbf{E} \right)_{ii} \frac{\mathbf{f}_k(\mathbf{u}_j) - \mathbf{f}_k(\mathbf{u}_i)}{2} - (\boldsymbol{\lambda}_k)_i (\mathbf{u}_j + \mathbf{u}_i) \\ + \left(\sum_{j \in \mathcal{I}(i)} 2\lambda_{ij} + \sum_{j \in \mathcal{B}(i)} \sum_{k=1}^2 2(\boldsymbol{\lambda}_k)_i \right) \mathbf{u}_i = 0 \end{aligned} \quad (23)$$

where we write \mathbf{u}_i^n as \mathbf{u}_i for simplicity of the notation. We define $\mathcal{I}(i)$, the neighboring nodes of node i , as the set of indices j where $\left(\mathbf{Q}_r^L - \left(\mathbf{Q}_r^L \right)^T \right)_{ij}$ or $\left(\mathbf{Q}_s^L - \left(\mathbf{Q}_s^L \right)^T \right)_{ij}$ is nonzero. $\mathcal{B}(i)$ is the set of indices on the exterior of the surface quadrature points, whose states are usually denoted by \mathbf{u}^+ .

Then, we can rearrange the equation and write the low order solution as a convex combination of the previous state \mathbf{u}^n and the intermediate states $\bar{\mathbf{u}}$:

$$\mathbf{u}_i^{L, n+1} = \left(1 - \frac{2\tau\lambda_i}{\mathbf{m}_i} \right) \mathbf{u}_i + \frac{2\tau\lambda_{ij}}{\mathbf{m}_i} \sum_{j \in \mathcal{I}(i)} \bar{\mathbf{u}}_{\mathbf{u}_i, \mathbf{u}_j, \boldsymbol{\sigma}_i, \boldsymbol{\sigma}_j, \mathbf{n}_{ij}} + \sum_{k=1}^2 \frac{2\tau(\boldsymbol{\lambda}_k)_i}{\mathbf{m}_i} \sum_{j \in \mathcal{B}(i)} \bar{\mathbf{u}}_{\mathbf{u}_i, \mathbf{u}_i^+, \boldsymbol{\sigma}_i, \boldsymbol{\sigma}_i^+, \mathbf{n}_i}, \quad (24)$$

where we define the intermediate states as

$$\bar{\mathbf{u}}_{\mathbf{u}_L, \mathbf{u}_R, \boldsymbol{\sigma}_L, \boldsymbol{\sigma}_R, \mathbf{n}} = \frac{1}{2} (\mathbf{u}_L + \mathbf{u}_R) - \frac{1}{2\alpha} \mathbf{n} \cdot (\mathbf{f}_R^I - \boldsymbol{\sigma}_R - \mathbf{f}_L^I + \boldsymbol{\sigma}_L). \quad (25)$$

We can show the intermediate states are admissible with the viscosity coefficients defined in (18).

Lemma 5.1. For admissible states $(\mathbf{u}_L, \mathbf{u}_R) \in \mathcal{A} \times \mathcal{A}$, the bar states $\bar{\mathbf{u}}_{\mathbf{u}_L, \mathbf{u}_R, \boldsymbol{\sigma}_L, \boldsymbol{\sigma}_R, \mathbf{n}}$ are admissible.

Proof. We can rewrite the intermediate state as

$$\bar{\mathbf{u}}_{\mathbf{u}_L, \mathbf{u}_R, \boldsymbol{\sigma}_L, \boldsymbol{\sigma}_R, \mathbf{n}} = \frac{1}{2\beta} [\beta \mathbf{u} + (\mathbf{f}^I(\mathbf{u}) - \boldsymbol{\sigma}) \cdot \mathbf{n}] + \frac{1}{2\beta} [\beta \mathbf{u} - (\mathbf{f}^I(\mathbf{u}) - \boldsymbol{\sigma}) \cdot \mathbf{n}], \quad (26)$$

and it is admissible by (20) [16]. \square

Then the conservation and positivity preserving properties of the formulation (16) directly follows from Lemma 5.1.

Theorem 5.2. Assume the domain is periodic. The formulation (16) is conservative

$$\mathbf{1}^T \mathbf{M} \mathbf{u}^{k+1} = \mathbf{1}^T \mathbf{M} \mathbf{u}^k. \quad (27)$$

In addition, if a timestep condition is satisfied

$$\tau \leq \frac{\mathbf{m}_i}{2\lambda_i}, \quad \lambda_i = \sum_{j \in \mathcal{I}(i)} \lambda_{ij} + \sum_{j \in \mathcal{B}(i)} \sum_{k=1}^2 (\lambda_k)_i, \quad (28)$$

the formulation is positivity preserving:

$$\mathbf{u}_i^{L, n+1} \in \mathcal{A} \quad \text{for all } i. \quad (29)$$

Proof. $\left(\mathbf{Q}_k^L - (\mathbf{Q}_k^L)^T \right) \circ \mathbf{F}_k$ and $\boldsymbol{\Lambda} \circ \mathbf{D}$ are skew-symmetric, so

$$\mathbf{1}^T \left[\sum_{k=1}^2 \left(\left(\mathbf{Q}_k^L - (\mathbf{Q}_k^L)^T \right) \circ \mathbf{F}_k \right) \mathbf{1} - (\boldsymbol{\Lambda} \circ \mathbf{D}) \mathbf{1} \right] = 0. \quad (30)$$

In addition, we assume the domain is periodic, so

$$\mathbf{1}^T \mathbf{E}^T \sum_{k=1}^2 (\mathbf{B}_k \mathbf{f}_k^* - \lambda_k \llbracket \mathbf{u} \rrbracket + \mathbf{B}_k^+ \mathbf{f}_k^* - \lambda_k \llbracket \mathbf{u}^+ \rrbracket) = 0, \quad (31)$$

the conservation property follows.

From 24, the low order update is an convex combination of admissible states if a timestep condition is satisfied: $\tau \leq \frac{\mathbf{m}_i}{2\lambda_i}$. Since the admissible set \mathcal{A} is convex, the low order update $\mathbf{u}_i^{L, n+1}$ is admissible. \square

6. Positivity limiting strategy

In this section, we will discuss the way to combine the robust low-order discretization with the high-order entropy-stable discretization. To simplify the notation, we adapt the notation used in [21], so we can write the low order and high-order approximations over node i in algebraic forms:

$$\mathbf{m}_i \frac{\mathbf{u}_i^{L, n+1} - \mathbf{u}_i}{\tau} + \sum_{j \in \mathcal{I}(i)} \mathbf{F}_{ij}^L + \sum_{j \in \mathcal{B}(i)} \mathbf{F}_{ij}^{B, L} = 0 \quad (32)$$

$$\mathbf{m}_i \frac{\mathbf{u}_i^{H, n+1} - \mathbf{u}_i}{\tau} + \sum_{j \in \mathcal{I}(i)} \mathbf{F}_{ij}^H + \sum_{j \in \mathcal{B}(i)} \mathbf{F}_{ij}^{B, H} = 0 \quad (33)$$

In particular, for the compressible Navier-Stokes equation, the low and high order algebraic fluxes are

$$\mathbf{F}_{ij}^L = \sum_{k=1}^2 \frac{1}{2} \left(\mathbf{Q}_k^L - (\mathbf{Q}_k^L)^T \right)_{ij} \left[\mathbf{f}_k(\mathbf{u}_i) + \mathbf{f}_k(\mathbf{u}_j) - (\boldsymbol{\sigma}_k)_i - (\boldsymbol{\sigma}_k)_j \right] - \lambda_{ij} (\mathbf{u}_j - \mathbf{u}_i), \quad (34)$$

$$\mathbf{F}_{ij}^{B,L} = \sum_{k=1}^2 \frac{1}{2} \left(\mathbf{E}^T \mathbf{B}_k \mathbf{E} \right)_{ii} \left[\mathbf{f}_k(\mathbf{u}_i) + \mathbf{f}_k(\mathbf{u}_i^+) - (\boldsymbol{\sigma}_k)_i - (\boldsymbol{\sigma}_k)_i^+ \right] - (\boldsymbol{\lambda}_k)_i (\mathbf{u}_i^+ - \mathbf{u}_i) \quad (35)$$

$$\mathbf{F}_{ij}^H = \sum_{k=1}^2 \left(\mathbf{Q}_k^L - (\mathbf{Q}_k^L)^T \right)_{ij} \left[\mathbf{f}_{k,S}(\mathbf{u}_i, \mathbf{u}_j) - \frac{(\boldsymbol{\sigma}_k)_i + (\boldsymbol{\sigma}_k)_j}{2} \right], \quad (36)$$

$$\mathbf{F}_{ij}^{B,H} = \sum_{k=1}^2 \left(\mathbf{E}^T \mathbf{B}_k \mathbf{E} \right)_{ii} \left[\mathbf{f}_{k,S}(\mathbf{u}_i, \mathbf{u}_i^+) - \frac{(\boldsymbol{\sigma}_k)_i + (\boldsymbol{\sigma}_k)_i^+}{2} \right] - \frac{\mathbf{w}_i^f(\boldsymbol{\lambda}_{\max,k})_i}{2} (\mathbf{u}_i^+ - \mathbf{u}_i), \quad (37)$$

and we can derive the low and high order algebraic fluxes for the compressible Euler equation by eliminating the viscous terms. We can establish the relation between the low and high order updates through the low and high order algebraic fluxes:

$$\mathbf{m}_i \mathbf{u}_i^{H,n+1} = \mathbf{m}_i \mathbf{u}_i^{L,n+1} + \tau \left(\sum_{j \in \mathcal{I}(i)} (\mathbf{F}_{ij}^L - \mathbf{F}_{ij}^H) + \sum_{j \in \mathcal{B}(i)} (\mathbf{F}_{ij}^{B,L} - \mathbf{F}_{ij}^{B,H}) \right) \quad (38)$$

6.1. Convex limiting

Inspired by flux corrected transport [41], the limited solution can be written as

$$\mathbf{m}_i \mathbf{u}_i^{n+1} = \mathbf{m}_i \mathbf{u}_i^{L,n+1} + \tau \left(\sum_{j \in \mathcal{I}(i)} l_{ij} (\mathbf{F}_{ij}^L - \mathbf{F}_{ij}^H) + \sum_{j \in \mathcal{B}(i)} l_{ij} (\mathbf{F}_{ij}^{B,L} - \mathbf{F}_{ij}^{B,H}) \right), \quad (39)$$

where l_{ij} are limiting parameters in the range $[0, 1]$. Following the idea in [20], we can rewrite the limited solution as a convex combination of substates of form $\mathbf{u} + l\mathbf{P}$:

$$\begin{aligned} \mathbf{u}_i^{n+1} &= \sum_{j \in \mathcal{I}(i)} \lambda_j (\mathbf{u}_i^{L,n+1} + l_{ij} \mathbf{P}_{ij}) + \sum_{j \in \mathcal{B}(i)} \lambda_j (\mathbf{u}_i^{L,n+1} + l_{ij} \mathbf{P}_{ij}^B), \\ \mathbf{P}_{ij} &= \frac{\tau}{\mathbf{m}_i \lambda_j} (\mathbf{F}_{ij}^L - \mathbf{F}_{ij}^H), \quad \mathbf{P}_{ij}^B = \frac{\tau}{\mathbf{m}_i \lambda_j} (\mathbf{F}_{ij}^{B,L} - \mathbf{F}_{ij}^{B,H}), \quad \sum_{j \in \mathcal{I}(i) \cup \mathcal{B}(i)} \lambda_j = 1, \quad \lambda_j > 0, \end{aligned} \quad (40)$$

where $\{\lambda_j\}_{\mathcal{I}(i) \cup \mathcal{B}(i)}$ is a set of strictly positive convex coefficients. For example, in the numerical experiments in this work, we will use one of the most obvious choices of convex coefficients: $\lambda_j = \frac{1}{\text{card}(\mathcal{I}(i) \cup \mathcal{B}(i))}$. In [21], other choices of convex coefficients are explored and they do not show significant advantages over the uniform choice.

Since the admissible set \mathcal{A} is convex, the limited solution lies in the admissible set if every sub-state of the form $\mathbf{u}^L + l\mathbf{P}$ is admissible. When the limiting parameter $l = 0$, we recover the admissible low order approximation, and when the limiting parameter $l = 1$, we recover the high order entropy-stable approximation, which may not be admissible. In order to stay as close to the high-order scheme as possible, we determine the value of limiting parameters by finding the largest possible l that satisfies the positivity constraints:

$$l_{ij} = \max \left\{ l \in [0, 1] \mid \mathbf{u}_i^{L,n+1} + l\mathbf{P}_{ij} \in \mathcal{A}, \quad \mathbf{u}_j^{L,n+1} + l\mathbf{P}_{ji} \in \mathcal{A} \right\}. \quad (41)$$

The constraint $\mathbf{u}_i^L + l\mathbf{P} \in \mathcal{A}$ is a quadratic constraint with respect to l . Solving the constraint for the internal energy reduces to solving a quadratic equation. We state the explicit formula of l here and refer

readers to [21] for details of the proof.

$$l^\rho = \begin{cases} 1 & \text{if } \rho^L + \rho^P \geq 0, \\ \max\left(\frac{-\rho^L + \epsilon_0}{\rho^P}, 0\right) & \text{otherwise,} \end{cases} \quad (42)$$

$$l^{\rho e} = \begin{cases} 1 & \text{if } \{l \geq 0 \mid al^2 + bl + c = 0\} = \emptyset, \\ \min\{l \geq 0 \mid al^2 + bl + c = 0\} & \text{otherwise,} \end{cases} \quad (43)$$

$$\begin{aligned} a &= E^P \rho^P - \frac{1}{2} \mathbf{m}^P \cdot \mathbf{m}^P, & b &= E^L \rho^P + \rho^L E^P - \mathbf{m}^L \cdot \mathbf{m}^P, & c &= E^L \rho^L - \frac{1}{2} \mathbf{m}^L \cdot \mathbf{m}^L - \epsilon_0, \\ l &= \min(l^\rho, l^{\rho e}). \end{aligned} \quad (44)$$

The limiting parameters l_{ij} are typically enforced to be symmetric citeguermond2019invariant, which ensures the following theorem:

Theorem 6.1. If $l_{ij} = l_{ji}$, the limited solution (39) is conservative and admissible.

Proof. If we choose limiting parameters according to (42), (43), and (44), the limiting solution \mathbf{u}_i^{n+1} is a convex combination of admissible sub-states by (40). Because the admissible set is a convex set, the limited solution is admissible. The conservation properties follow from the symmetry of the limiting parameters $l_{ij} = l_{ji}$ [21]. \square

6.2. Localization of the limiting parameters

Symmetrizing the limiting parameters in (41) ensures the conservation property of the limited solution. However a naive implementation of symmetrization requires the exchange of information on neighboring elements. We propose to use Lax-Friedrichs type interface fluxes in our high order ESDG formulation, which avoids this exchange of information and localizes the convex limiting procedure.

When wave speeds are suitably chosen, the Lax-Friedrichs fluxes are entropy- stable, and as a result the high-order entropy-stable discretizations with Lax-Friedrichs flux on the interfaces are entropy-stable [42] too. Then, for the compressible Euler and Navier-Stokes equations, the interface numerical fluxes of the high order entropy stable methods are identical to the interface numerical fluxes of the low-order scheme:

$$\mathbf{F}_{ij}^{\text{B,H}} = \mathbf{F}_{ij}^{\text{B,L}} = \sum_{k=1}^2 \frac{1}{2} \left(\mathbf{E}^T \mathbf{B}_k \mathbf{E} \right)_{ii} \left[\mathbf{f}_k(\mathbf{u}_i) + \mathbf{f}_k(\mathbf{u}_i^+) - (\sigma_k)_i - (\sigma_k)_i^+ \right] - (\lambda_k)_i (\mathbf{u}_i^+ - \mathbf{u}_i). \quad (45)$$

Since the low and high order algebraic fluxes are identical on the interface, the limited solution can be written in terms of only low and high order algebraic fluxes in the interior of the element:

$$\mathbf{m}_i \mathbf{u}_i^{n+1} = \mathbf{m}_i \mathbf{u}_i^{\text{L},n+1} + \tau \sum_{j \in \mathcal{I}(i)} l_{ij} \left(\mathbf{F}_{ij}^{\text{L}} - \mathbf{F}_{ij}^{\text{H}} \right). \quad (46)$$

The high-order method is still entropy stable, as shown in [10, 43].

We note that this localization property is not specific to the Lax-Friedrichs flux, and that convex limiting reduces to a local procedure for any high and low order schemes which share the same interface flux and interface discretization matrices.

6.3. Limiting strategies

In this section, we will present three limiting strategies. The limited solutions are all of form (46). The choice of limiting parameters l_{ij} distinguishes these strategies.

6.3.1. Nodal limiting

We refer the limiting strategy as *Nodal limiting strategy* if the limiting parameters l_{ij} are defined as in (41), since the limiting parameters depend on the nodes.

This strategy is adopted in [20, 21, 29], and can be advantageous because it offers sub-cell “blending” of high and low order schemes in addition to any sub-cell resolution provided by the low order positivity-preserving scheme. However, in this work we only enforce minimal positivity conditions (i.e., global positivity of density and internal energy), while previous literature used convex-limiting to enforce stronger constraints (e.g. local bounds-preservation on density and local minimum principle on the specific entropy).

We note that the other limiting strategies considered in this work utilize a single blending parameter on each element, which naturally preserves a semi-discrete cell entropy inequality. In contrast, the nodal limiting strategy can not be shown to preserve a semi-discrete cell entropy inequality. The lack of a numerical entropy inequality has been shown to introduce spurious phenomena [44], and Appendix A shows some examples of potentially spurious phenomena using nodal limiting. Future work will include a more detailed investigation of non-entropic behaviors using nodal limiting.

6.3.2. Elementwise (Zalesak-type) limiting

The modification of the interface numerical flux of the high-order method in Section 6.2 allows us to limit the solution in an elementwise fashion:

$$l_{ij} = \max \{ l \in [0, 1] \mid \mathbf{u}_m^{L,n+1} + l\mathbf{P}_{mn} \in \mathcal{A}, \quad m, n \in \mathcal{K}(i) \}, \quad (47)$$

where $\mathcal{K}(i)$ is the set of indices in the same element as node i . By construction, the limiting parameter is constant over each element, and it is the largest $l \in [0, 1]$ that make all substates of form $\mathbf{u}^L + l\mathbf{P}$ within the element admissible. We call this strategy *Elementwise (Zalesak-type) limiting* [45].

As will be shown in Section 8.1.3, Elementwise (Zalesak-type) limiting tends to activate limiting even when the high-order solution is positive. As a result, we can observe low-order accuracy even for well-behaved smooth problems. This is due to the fact that the limiting parameters are determined based on individual entries of SBP operators, which can apply limiting in an element even if the high-order solution is positive. We alleviate this problem by using the following approach: in our implementation, we introduce a positivity detector so that we activate the limiting at an element only when the high order approximation over this element has negative values. In particular,

$$\mathbf{u}_i \in \mathcal{A} \text{ for all } i \in D^k \implies l_{ij} = 1 \text{ for all } i, j \in D^k. \quad (48)$$

As we verify in Section 8, the positivity detector recovers the high order convergence of entropy stable discretizations in smooth regions.

6.3.3. Elementwise (Zhang-Shu type) limiting

We consider a more optimistic construction of the elementwise limiting parameter, as introduced in [14, 29]. We can define the new limiting parameter using l_i^e :

$$l_i^e = \max \left\{ l \in [0, 1] \mid \mathbf{u}_i^{L,n+1} + l \frac{\tau}{\mathbf{m}_i} \sum_{j \in \mathcal{I}(i)} (\mathbf{F}_{ij}^L - \mathbf{F}_{ij}^H) \in \mathcal{A} \right\}, \quad (49)$$

and then the new limiting parameter l_{ij} can be written as

$$l_{ij} = \min \{ l_m^e \mid m \in \mathcal{K}(i) \}. \quad (50)$$

Like the Zalesak-type limiter, this limiting parameter is also constant over each element. We call this *Elementwise (Zhang-Shu type) limiting*.

Elementwise (Zalesak-type) limiting (47) is a more pessimistic positivity limiting strategy compared to Elementwise (Zhang-Shu type) limiting (49), since its limiting parameters depend on the nodewise interactions of algebraic fluxes within elements. On the other hand, Elementwise (Zhang-Shu type) limiting disregards the interactions between algebraic fluxes, and instead focuses on finding the largest limiting coefficients (49) that ensure the positivity of the limited solution at individual nodes.

6.4. Entropy stable and positivity preserving limiting strategies

We can, in addition, show the low-order positivity preserving method in Section 5 is discretely entropy-stable if we modify the amount of dissipation α :

Theorem 6.2. If we define the viscosity coefficients as

$$\alpha(\mathbf{u}_L, \mathbf{u}_R, \boldsymbol{\sigma}_L, \boldsymbol{\sigma}_R, \mathbf{n}) = \max(\lambda_{\max}(\mathbf{u}_L, \mathbf{u}_R, \mathbf{n}), \beta(\mathbf{u}_L, \boldsymbol{\sigma}_L, \mathbf{n}), \beta(\mathbf{u}_R, \boldsymbol{\sigma}_R, \mathbf{n})), \quad (51)$$

then the positivity preserving method (16) satisfies a discrete entropy balance

$$\mathbf{v}^T \mathbf{M} \frac{\partial \mathbf{u}}{\partial t} \leq \sum_{k=1}^2 \left[\mathbf{1}^T \mathbf{E}^T \mathbf{B}_k \mathbf{E} \psi_k \right] - \mathbf{v}^T \mathbf{E}^T \mathbf{W}_f \hat{\mathbf{f}}^* - \sum_{i,j=1}^2 \boldsymbol{\Theta}_i^T \mathbf{M} \mathbf{K}_{ij} \boldsymbol{\Theta}_j, \quad (52)$$

where $\boldsymbol{\Theta} = 0$ for the compressible Euler equation.

Proof. We test the formulation (21) with entropy variables \mathbf{v} evaluated at nodes. We can rewrite the volume contribution as [4]

$$-\mathbf{v}^T \left(2 \|\mathbf{n}_{ij}\| \circ \hat{\mathbf{F}} \right) \mathbf{1} = -\mathbf{v}^T \left(\|\mathbf{n}_{ij}\| \circ \hat{\mathbf{F}} \right) \mathbf{1} + \mathbf{v}^T \left(\|\mathbf{n}_{ij}\| \circ \hat{\mathbf{F}}^T \right) \mathbf{1} \quad (53)$$

$$= \sum_{i,j} \|\mathbf{n}_{ij}\| (\mathbf{v}_i - \mathbf{v}_j)^T \hat{\mathbf{f}} \left(\mathbf{u}_i, \mathbf{u}_j, \frac{\mathbf{n}_{ij}}{\|\mathbf{n}_{ij}\|} \right) \quad (54)$$

$$\leq \sum_{i,j} \|\mathbf{n}_{ij}\| \frac{\mathbf{n}_{ij}}{\|\mathbf{n}_{ij}\|} \cdot (\psi_i - \psi_j) \quad (55)$$

$$= \sum_{k=1}^2 \mathbf{1}^T \left(\frac{\mathbf{E}^T \mathbf{B}_k \mathbf{E}}{2} - \mathbf{Q}_k^T \right) \psi_k - \psi_k^T \left(\mathbf{Q}_k - \frac{\mathbf{E}^T \mathbf{B}_k \mathbf{E}}{2} \right) \mathbf{1} = \sum_{k=1}^2 \left[\mathbf{1}^T \mathbf{E}^T \mathbf{B}_k \mathbf{E} \psi_k \right], \quad (56)$$

where we used the skew-symmetry of $\hat{\mathbf{F}}$ and the SBP property of \mathbf{Q} . From (54) to (55), we have used the entropy stability of the Lax-Friedrichs flux:

$$(\mathbf{v}_i - \mathbf{v}_j)^T \hat{\mathbf{f}} \leq \psi_i - \psi_j. \quad (57)$$

The surface contribution $-\mathbf{v}^T \mathbf{E}^T \mathbf{W}_f \hat{\mathbf{f}}^*$ directly follows from rearrangement, and the viscous contribution $-\sum_{i,j=1}^2 \boldsymbol{\Theta}_i^T \mathbf{M} \mathbf{K}_{ij} \boldsymbol{\Theta}_j$ follows from [6]. \square

We note that for the compressible Euler equations, the viscosity coefficient β defined in (19) is never larger than the maximum wavespeed. Therefore, the modified viscosity coefficient α defined in (51) reduces to the standard maximum wavespeed estimate for compressible Euler.

As a result of Theorem 6.3, the limited solutions using Elementwise (Zalesak-type) limiting or Elementwise (Zhang-Shu type) limiting introduced in Section 6.3.2 and 6.3.3 both satisfy a semi-discrete entropy balance.

Theorem 6.3. Assume the domain is periodic. The elementwise limited solution \mathbf{u}^{n+1} is conservative, positivity preserving, satisfy the discrete entropy dissipation for the compressible Euler equation,

$$\mathbf{v}^T \mathbf{M} \frac{\partial \mathbf{u}^{n+1}}{\partial t} \leq 0, \quad (58)$$

and satisfy the discrete entropy balance for the compressible Navier-Stokes equation,

$$\mathbf{v}^T \mathbf{M} \frac{\partial \mathbf{u}^{n+1}}{\partial t} \leq - \sum_{i,j=1}^2 \boldsymbol{\Theta}_i^T \mathbf{M} \mathbf{K}_{ij} \boldsymbol{\Theta}_j \quad (59)$$

Proof. Over each element, the elementwise limited solution can be written as a linear combination of low and high order solutions:

$$\mathbf{u}_i^{n+1} = (1-l) \mathbf{u}^{L,n+1} + l \mathbf{u}^{H,n+1}, \quad (60)$$

where l is the elementwise limiting parameter. The result follows from the fact that both high and low-order solutions satisfy the discrete entropy balances [10, 7]. \square

7. Time discretization

Until now, we have assumed a first order forward Euler time discretization. We extend to higher order in time using Strong Stability Preserving (SSP) explicit time stepping schemes. We present here the SSPRK(3,3) method for reference.

$$\begin{aligned} w^{(1)} &= u^n + \tau L(t^n, u^n), & z^{(1)} &= w^{(1)} + \tau L(t^n + \tau, w^{(1)}) \\ w^{(2)} &= \frac{3}{4}u^n + \frac{1}{4}z^{(1)}, & z^{(2)} &= w^{(2)} + \tau L(t^n + \frac{1}{2}\tau, w^{(2)}), \\ u^{n+1} &= \frac{1}{3}u^n + \frac{2}{3}z^{(2)} \end{aligned}$$

where τ is the timestep size, and $L(t, u)$ is the evaluation of the time derivative.

The limiting framework we propose ensures the solution remains in the convex admissible set (3) for a single forward Euler timestep. Since SSP schemes are the convex combinations of first-order forward Euler steps, any convex set will be preserved [46].

8. Numerical experiments

In this section, we present various numerical experiments to verify the convergence and robustness of the proposed limiting strategy ³. All of the simulations advance in time using the third-order SSP Runge Kutta method introduced in Section 7. The timestep size is determined from the timestep condition in (28):

$$\Delta t = \text{CFL} \min_i \frac{\mathbf{m}_i}{2\lambda_i}, \quad (61)$$

where CFL is a user specified parameter. For all numerical experiments, we set the positivity threshold as $\epsilon_0 = 10^{-14}$ in (19) and (44). All the limiting strategies use the modified viscosity coefficients introduced in Theorem 6.2. We estimate the maximum wavespeed associated with the 1D Riemann problems by the Rusanov estimate

$$\lambda_{\max}(\mathbf{u}_L, \mathbf{u}_R, \mathbf{n}) = \max \left(|\mathbf{u}_L \cdot \mathbf{n}| + \sqrt{\gamma \frac{p_L}{\rho_L}}, |\mathbf{u}_R \cdot \mathbf{n}| + \sqrt{\gamma \frac{p_R}{\rho_R}} \right). \quad (62)$$

The entropy stable schemes in this work utilize the entropy conservative numerical flux introduced by Chandreshekar [39]. We evaluate the logarithmic mean with Ismail and Roe's approach [47] to avoid numerical instability.

For all numerical experiments on simplicial elements, we construct sparse low order SBP operators by building the adjacency matrix and graph Laplacian in equation (11) with $\beta = 1$ and $\alpha = 4, 2.5, 3.5, 3.5$ for polynomial degrees $N = 1, 2, 3, 4$ respectively. We note that the selection of parameters are not optimal, and numerical results are not sensitive to the choice of the parameters.

³The codes used for the experiments are available at <https://github.com/yiminlin/ESDG-PosLimit/tree/main/examples/IDP>

8.1. Convergence tests

The high order accuracy of the high order entropy stable discretizations has already been shown in [7, 4], and the convergence of low order positivity preserving methods for the compressible Euler equations was explored in detail in [19, 29]. Thus, in this section, we focus on studying the behaviour of the Elementwise (Zalesak-type) limiting and Nodal limiting strategies on test cases where the entropy stable discretization fails due to the loss of positivity.

We also note that the high order convergence of Elementwise (Zhang-Shu type) limiting is thoroughly studied in [14, 16]. We also performed the same set of numerical experiments in this section on Zhang-Shu type limiting and observe high order convergence for smooth problems. For these reasons, we do not include the numerical experiments with Zhang-Shu type limiting in this section for brevity.

All of tests cases in this section have exact solutions, and we evaluate the relative L^p errors of conservative variables using quadrature:

$$\frac{[\mathbf{1}^T \mathbf{M}(\rho^n - \rho)^p]^{1/p}}{[\mathbf{1}^T \mathbf{M} \rho^p]^{1/p}} + \frac{[\mathbf{1}^T \mathbf{M}(\rho u^n - \rho u)^p]^{1/p}}{[\mathbf{1}^T \mathbf{M}(\rho u)^p]^{1/p}} + \frac{[\mathbf{1}^T \mathbf{M}(\rho v^n - \rho v)^p]^{1/p}}{[\mathbf{1}^T \mathbf{M}(\rho v)^p]^{1/p}} + \frac{[\mathbf{1}^T \mathbf{M}(E^n - E)^p]^{1/p}}{[\mathbf{1}^T \mathbf{M} E^p]^{1/p}}, \quad (63)$$

where the numerical solutions and exact solutions evaluated at quadrature nodes are denoted by \mathbf{u}^n and \mathbf{u} respectively.

8.1.1. Leblanc shocktube

We first consider the Leblanc shocktube problem for the compressible Euler equation. This is a challenging Riemann problem and entropy stable discretizations fail due to negative density and pressure at the shock. The domain is $[0, 1]$, and the initial condition in primitive variables is

$$\mathbf{u}_0(x) = \begin{cases} \mathbf{u}_L, & x < x_0 \\ \mathbf{u}_R, & \text{otherwise} \end{cases}, \quad \mathbf{u}_L = \begin{bmatrix} \rho_L \\ u_L \\ p_L \end{bmatrix} = \begin{bmatrix} 1.0 \\ 0.0 \\ (\gamma - 1) 0.1 \end{bmatrix}, \quad \mathbf{u}_R = \begin{bmatrix} \rho_R \\ u_R \\ p_R \end{bmatrix} = \begin{bmatrix} 10^{-3} \\ 0.0 \\ (\gamma - 1) 10^{-10} \end{bmatrix}, \quad (64)$$

where $x_0 = 0.33, \gamma = \frac{5}{3}$. We set the exterior values at endpoints of the domain $x = 0, 1$ to be $\mathbf{u}_L, \mathbf{u}_R$ to enforce inhomogeneous Dirichlet boundary condition. The test case has an exact solution of form [19]

$$\mathbf{u}(x) = \begin{cases} \mathbf{u}_L, & \xi \leq -\frac{1}{3} \\ \begin{pmatrix} \rho^{**} & v^{**} & p^{**} \end{pmatrix} & -\frac{1}{3} < \xi \leq \lambda_1 \\ \begin{pmatrix} \rho_L^* & v^* & p^* \end{pmatrix} & \lambda_1 < \xi \leq v^* \\ \begin{pmatrix} \rho_R^* & v^* & p^* \end{pmatrix} & v^* < \xi \leq \lambda_3 \\ \mathbf{u}_R, & \lambda_3 < \xi \end{cases}, \quad (65)$$

$$\begin{aligned} \rho^{**} &= (0.75 - 0.75\xi)^3, & v^{**} &= 0.75 \left(\frac{1}{3} + \xi \right), & p^{**} &= \frac{1}{15} (0.75 - 0.75\xi)^5, \\ \rho_L^* &= 5.40793353493162 \times 10^{-2}, & \rho_R^* &= 3.99999806043000 \times 10^{-3}, & p^* &= 0.515577927650970 \times 10^{-3}, \\ v^* &= 0.621838671391735, & \lambda_1 &= 0.495784895188979, & \lambda_3 &= 0.829118362533470, \end{aligned}$$

where $\xi = \frac{x-x_0}{t}$. We discretize the domain by uniform intervals, set $\text{CFL} = 0.5$, and run the simulations until $T = 2/3$. We calculate the L^1 errors of different strategies with the order of approximation $N = 2, 5$, and we discretize the mesh with K uniform intervals.

We compare the L^1 error and the convergence rate of the low order solution, the solutions using Elementwise (Zalesak-type) limiting with and without positivity detection, and the solutions using Nodal limiting strategy. As Table 1 shows, all strategies are first order accurate, which is optimal for this test case. Figure 2 compares two different Elementwise (Zalesak-type) limited solutions with positivity detection when the

degrees of freedom is 600. We observe higher order approximation gives less oscillatory solutions, and it generates more accurate results from Table 1d. In addition, Figure 3 compares low order solutions when the degrees of freedom is 600. The results are nearly identical for polynomial degrees $N = 2$ and $N = 5$. The results of table 1a verify that the accuracy of low-order solutions using the sparse SBP operators does not degrade as we increase the polynomial order [29].

K	Low order, $N = 2$		Low order, $N = 5$	
	L^1 error	Rate	L^1 error	Rate
50	2.115×10^{-1}		1.705×10^{-1}	
100	1.664×10^{-1}	0.35	1.116×10^{-1}	0.61
200	1.117×10^{-1}	0.57	7.382×10^{-2}	0.60
400	7.275×10^{-2}	0.62	4.627×10^{-2}	0.67
800	4.610×10^{-2}	0.66	2.868×10^{-2}	0.69

(a) Low order method

K	Limited, $N = 2$		Limited, $N = 5$	
	L^1 error	Rate	L^1 error	Rate
50	8.012×10^{-2}		5.538×10^{-2}	
100	3.360×10^{-2}	1.25	1.292×10^{-2}	2.10
200	1.410×10^{-2}	1.25	4.331×10^{-3}	1.58
400	6.437×10^{-3}	1.13	1.455×10^{-3}	1.57
800	3.016×10^{-3}	1.09	8.310×10^{-4}	0.81

(b) Nodal limiting

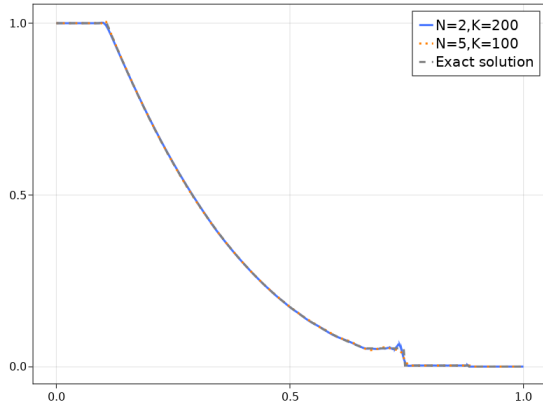
K	Limited, $N = 2$		Limited, $N = 5$	
	L^1 error	Rate	L^1 error	Rate
50	7.861×10^{-2}		5.143×10^{-2}	
100	3.403×10^{-2}	1.21	1.176×10^{-2}	2.13
200	1.428×10^{-2}	1.25	3.952×10^{-3}	1.57
400	6.622×10^{-3}	1.11	1.468×10^{-3}	1.43
800	3.101×10^{-3}	1.00	7.620×10^{-4}	0.95

(c) Elementwise (Zalesak-type) limiting with positivity detection

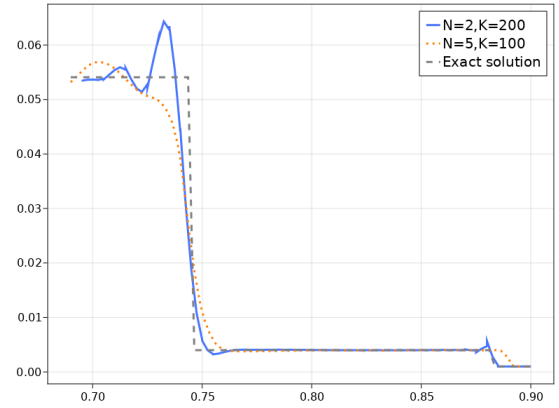
K	Limited, $N = 2$		Limited, $N = 5$	
	L^1 error	Rate	L^1 error	Rate
50	7.839×10^{-2}		5.086×10^{-2}	
100	3.303×10^{-2}	1.25	1.675×10^{-2}	1.60
200	1.369×10^{-2}	1.27	4.660×10^{-3}	1.85
400	6.251×10^{-3}	1.13	1.596×10^{-3}	1.55
800	2.960×10^{-3}	1.08	8.709×10^{-4}	0.87

(d) Elementwise (Zalesak-type) limiting without positivity detection

Table 1: Leblanc shocktube convergence tables



(a) Solutions



(b) Zoom in view

Figure 2: Leblanc shocktube, Elementwise (Zalesak-type) limiting with positivity detection

8.1.2. Viscous shockwave

We then consider a viscous shocktube problem for the compressible Navier-Stokes equations [22]. The test case starts from a steady state solution of the compressible Navier-Stokes equation, and we translate

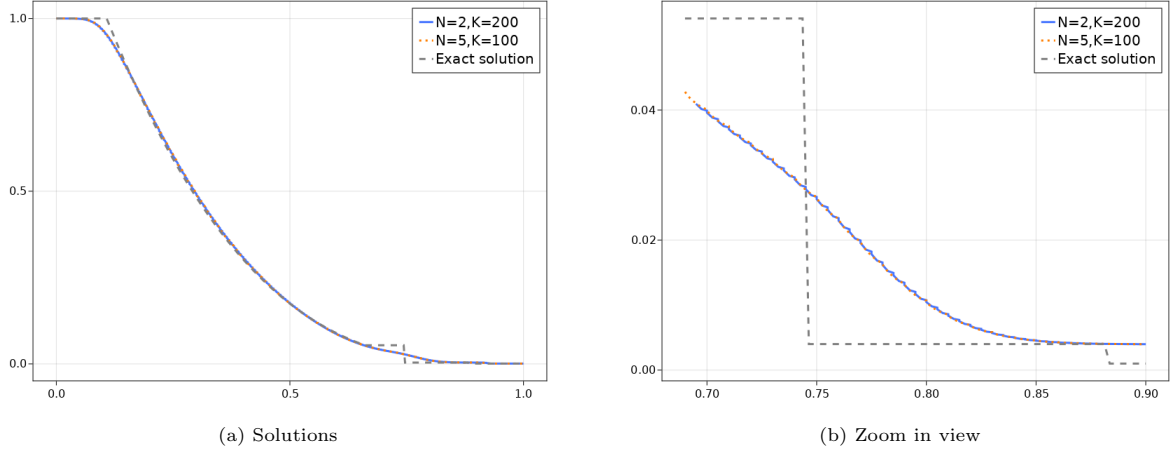


Figure 3: Leblanc shocktube, low order solutions

the solution with constant velocity u_∞ . The domain is $[-1, 1.5]$, and the analytical solution is defined as

$$\mathbf{u}(x, t) = \begin{bmatrix} \rho(\xi) \\ \rho(\xi)(u_\infty + u(\xi)) \\ \rho(\xi)\left(e(\xi) + \frac{1}{2}(u_\infty + u(\xi))^2\right) \end{bmatrix}, \quad \xi = x - u_\infty t, \quad (66)$$

$$\rho(x) = \frac{m_0}{u(x)}, \quad e(x) = \frac{1}{2\gamma} \left(\frac{\gamma+1}{\gamma-1} u_0^2 - u(x)^2 \right),$$

where the velocity profile $u(x)$ is defined implicitly by the equation

$$x = \frac{2\kappa}{(\gamma+1)m_0} \left[\frac{u_L}{u_L - u_R} \log \left(\frac{u_L - u(x)}{u_L - u_0} \right) - \frac{u_R}{u_L - u_R} \log \left(\frac{u(x) - u_R}{u_0 - u_R} \right) \right]. \quad (67)$$

Here, u_L, u_R denote the velocity at $-\infty, \infty$ respectively. We assume the velocity at ∞ depends on the pre-shock Mach number M_0 , $u_R = \frac{\gamma-1+2/M_0^2}{\gamma+1}$. We define $u_0 = \sqrt{u_L u_R}$ and $\text{Pr} = \frac{3}{4}$.

First, we verify the convergence of the low order positivity preserving discretizations. We set the parameters as follow: $\gamma = 1.4, \mu = 0.01, u_\infty = 0.2, u_L = 1.0, m_0 = 1.0, M_0 = 3$. We enforce inhomogeneous Dirichlet boundary condition on boundaries. We discretize the domain into uniform intervals, set $\text{CFL} = 0.5$, and run each simulation until $T = 1.0$. We compute the L^1 and L^2 errors of the low order positivity-preserving scheme. As Table 2 shown, the low-order method is first order accurate for $N = 2, 3, 4$.

Next we verify the convergence of the elementwise limited solutions. In this case, we set the parameters as: $\gamma = 1.4, \mu = 0.001, u_\infty = 0.2, u_L = 1.0, m_0 = 1.0, M_0 = 20.0$ and enforce the inhomogeneous Dirichlet boundary condition on boundaries. Using this set of parameters, the high-order entropy-stable discretizations will fail due to negative density and pressure when the mesh is sufficiently coarse. We discretize the domain by uniform intervals, set $\text{CFL} = 0.5$, and run the simulations until $T = 1.0$.

We compare the L^1 error and the convergence rate of the low-order solution, the solutions using Elementwise (Zalesak-type) limiting with and without positivity detection, and the solutions using Nodal-limiting strategy. As Table 3a shows, the low order solution is first order accurate. Nodal limiting and elementwise limiting solutions yield between $O(h^N)$ and $O(h^{N+1/2})$ convergence rates when the limiting is activated on coarse meshes. When $K = 1600$, the limited solutions are the same as high order ESDG solutions, for which we have verified high order convergence in [6]. Figure 4a compares different Elementwise (Zalesak-type) limited solutions with positivity detection when the degrees of freedom is 1200. As in the Leblanc shocktube test case, we observe higher-order approximation gives less oscillatory solutions, and the low order solutions are nearly identical with the same degrees of freedom.

$N = 2$				
K	L^1 error	Rate	L^2 error	Rate
50	7.69×10^{-2}		1.73×10^{-1}	
100	3.98×10^{-2}	0.95	1.05×10^{-1}	0.72
200	2.17×10^{-2}	0.87	6.34×10^{-2}	0.73
400	1.14×10^{-2}	0.93	3.62×10^{-2}	0.81
$N = 3$				
50	5.97×10^{-2}		1.42×10^{-1}	
100	3.32×10^{-2}	0.84	9.01×10^{-2}	0.66
200	1.70×10^{-2}	0.96	5.21×10^{-2}	0.79
400	8.70×10^{-3}	0.97	2.86×10^{-2}	0.86
$N = 4$				
50	5.16×10^{-2}		1.26×10^{-1}	
100	2.70×10^{-2}	0.93	7.70×10^{-2}	0.71
200	1.39×10^{-2}	0.96	4.37×10^{-2}	0.82
400	7.09×10^{-3}	0.97	2.36×10^{-2}	0.89

Table 2: $M_0 = 3$, Low order solutions

Low order, $N = 2$			Low order, $N = 3$		Limited, $N = 2$			Limited, $N = 3$	
K	L^1 error	Rate	L^1 error	Rate	K	L^1 error	Rate	L^1 error	Rate
50	9.000×10^{-2}		7.061×10^{-2}		50	8.146×10^{-2}		4.249×10^{-2}	
100	4.739×10^{-2}	0.93	3.711×10^{-2}	0.92	100	4.264×10^{-2}	0.93	2.178×10^{-2}	0.96
200	2.455×10^{-2}	0.95	1.939×10^{-2}	0.94	200	1.358×10^{-2}	1.65	4.698×10^{-3}	2.21
400	1.281×10^{-2}	0.94	1.006×10^{-2}	0.95	400	3.578×10^{-3}	1.92	7.870×10^{-4}	2.58
800	6.599×10^{-3}	0.96	5.179×10^{-3}	0.96	800	5.756×10^{-4}	2.63	1.163×10^{-4}	2.76
1600	3.394×10^{-3}	0.96	2.699×10^{-3}	0.94	1600	8.836×10^{-5}	2.70	1.269×10^{-5}	3.19

(a) Low order method

(b) Nodal limiting

Limited, $N = 2$			Limited, $N = 3$		Limited, $N = 2$			Limited, $N = 3$	
K	L^1 error	Rate	L^1 error	Rate	K	L^1 error	Rate	L^1 error	Rate
50	7.524×10^{-2}		5.181×10^{-2}		50	4.478×10^{-2}		4.431×10^{-2}	
100	4.228×10^{-2}	0.83	3.473×10^{-2}	0.58	100	2.545×10^{-2}	0.82	1.677×10^{-2}	1.40
200	1.768×10^{-2}	1.26	1.122×10^{-2}	1.63	200	1.306×10^{-2}	0.96	5.832×10^{-3}	1.52
400	3.646×10^{-3}	2.28	9.696×10^{-4}	3.53	400	3.714×10^{-3}	1.80	9.556×10^{-3}	2.60
800	5.768×10^{-4}	2.66	1.163×10^{-4}	3.06	800	5.775×10^{-4}	2.69	1.163×10^{-4}	3.04
1600	8.836×10^{-5}	2.71	1.269×10^{-5}	3.19	1600	8.836×10^{-5}	2.70	1.269×10^{-5}	3.19

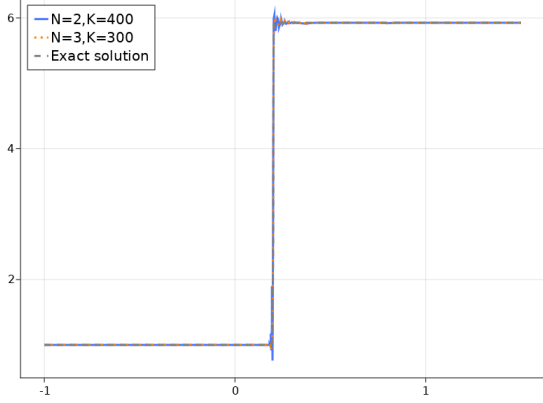
(c) Elementwise (Zalesak-type) limiting with positivity detection

(d) Elementwise (Zalesak-type) limiting without positivity detection

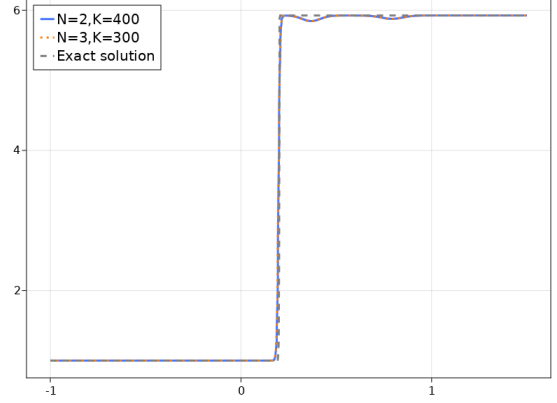
Table 3: Viscous shockwave convergence tables

8.1.3. Isentropic vortex

We now test the convergence of the limited solutions in 2D. Theorem 6.3 indicates that the elementwise limited solutions satisfy discrete entropy balances, but one cannot prove a similar result for nodal limited solutions. We will present numerical results in Appendix A (see Figures 11 and 12) where the nodal limiting strategy potentially produces non-entropic behaviors. The issue can be resolved by enforcing the minimum principle on specific entropy in addition to the positivity constraint [19]. However, since the focus of this work is on entropy stable schemes with a minimal positivity limiting strategy, we switch our focus to Elementwise (Zalesak-type) limiting with and without positivity detection in the following section.



(a) Elementwise (Zalesak-type) limiting with positivity detection



(b) Low order solution

Figure 4: Viscous shockwave

We examine the convergence of the elementwise limited solutions in 2D using the isentropic vortex test case [46]. The domain is $[0, 20] \times [0, 10]$, and the exact solution in primitive variables is defined as

$$\mathbf{u}(x, t) = \begin{bmatrix} \rho(x, t) \\ u(x, t) \\ v(x, t) \\ p(x, t) \end{bmatrix} = \begin{bmatrix} \left[1 - \frac{1}{8\gamma\pi^2} \left(.5(\gamma - 1) \left(\beta e^{1-r(x,t)^2} \right)^2 \right) \right]^{1/(\gamma-1)} \\ 1 - \frac{\beta}{2\pi} e^{1-r(x,t)^2} (y - y_0) \\ \frac{\beta}{2\pi} e^{1-r(x,t)^2} (y - y_0) \\ \rho(x, t)^\gamma \end{bmatrix}, \quad r(x, t) = \sqrt{(x - x_0 - t)^2 + (y - y_0)^2}, \quad (68)$$

where $(x_0, y_0) = (9.0, 5.0)$ denotes the center of the vortex at time $t = 0$, and $\beta = 8.5$ denotes strength of the vortex. Most numerical experiments in the literature choose the strength of the vortex $\beta = 5$, and the minimum density is 0.36 [4]. If $\beta = 8.5$, the entropy stable discretization fails due to large jumps in the density and pressure. For example, the maximum and minimum density in this test case are 1.0 and 2.145×10^{-3} , respectively.

We first test the convergence of the solutions on quadrilateral elements. We construct the mesh by discretizing the x, y directions with uniform $2K_{1D}, K_{1D}$ intervals, and this produces a bisected mesh with uniform quadrilateral elements. We enforce periodic boundary conditions on the domain and run the simulations until $T = 2.0$ with $\text{CFL} = 0.9$. Table 4 shows the elementwise limited solutions have asymptotic convergence rates between $O(h^{N+1/2})$ and $O(h^{N+1})$, which is optimal for smooth solutions. We plot the limiting parameters l_{ij} over each element at $T = 0.25$ with $N = 4, K_{1D} = 16$ in Figure 5a. The plot indicates the limiting is only activated at a single element where sharp jumps in density occur. We also observe that limiting is rarely activated throughout the simulation. This explains the optimal convergence rate of the elementwise limiting solutions with positivity detection.

On the other hand, Table 5 shows the Elementwise (Zalesak-type) limited solutions without positivity detection on quadrilateral meshes have asymptotic convergence rates between $O(h^{N+1/2})$ and $O(h^{N+1})$ for $N = 1, 2, 3$, but have only $O(h^{2.5})$ convergence rate when $N = 4$. We plot the limiting parameters l_{ij} over each element at $T = 1.0$ with $N = 4, K_{1D} = 16$ in Figure 6a. Compared with Elementwise limiting with positivity detection in Figure 5a, we observe the limiting are activated on more elements when the polynomial order is large, and the limiting is activated more frequently throughout the simulation.

	$N = 1$		$N = 2$		$N = 3$		$N = 4$	
K_{1D}	L^1 error	Rate	L^1 error	Rate	L^1 error	Rate	L^1 error	Rate
2	2.625×10^0		2.111×10^0		3.336×10^0		1.588×10^0	
4	1.982×10^0	0.41	2.023×10^0	0.06	8.625×10^{-1}	1.95	4.891×10^{-1}	1.70
8	1.559×10^0	0.35	0.625×10^{-1}	1.70	1.676×10^{-1}	2.36	9.222×10^{-2}	2.41
16	8.620×10^{-1}	0.86	1.058×10^{-2}	2.56	2.107×10^{-2}	2.99	7.355×10^{-3}	3.65
32	3.349×10^{-1}	1.36	1.404×10^{-3}	2.91	1.758×10^{-3}	3.58	1.312×10^{-4}	5.81

Table 4: Isentropic vortex, quadrilateral mesh - Elementwise (Zalesak-type) limiting with positivity detection

	$N = 1$		$N = 2$		$N = 3$		$N = 4$	
K	L^1 error	Rate	L^1 error	Rate	L^1 error	Rate	L^1 error	Rate
2	2.625×10^0		2.111×10^0		2.834×10^0		1.494×10^0	
4	1.982×10^0	0.41	1.955×10^0	0.11	9.281×10^{-1}	1.61	7.104×10^{-1}	1.07
8	1.541×10^0	0.36	6.833×10^{-1}	1.52	3.239×10^{-1}	1.52	3.193×10^{-1}	1.15
16	8.602×10^{-1}	0.84	1.447×10^{-1}	2.24	8.068×10^{-2}	2.01	8.047×10^{-2}	1.99
32	3.347×10^{-1}	1.36	2.356×10^{-2}	2.62	7.469×10^{-3}	3.43	1.148×10^{-2}	2.64

Table 5: Isentropic vortex, quadrilateral mesh - Elementwise (Zalesak-type) limiting without positivity detection

We then test convergence on simplicial elements. We construct each simplicial mesh by subdividing each element in the uniform quadrilateral mesh into two uniform triangles. We enforce periodic boundary conditions on the domain and run the simulations until $T = 2.0$ with $CFL = 0.5$. Table 6 shows the optimal convergence rate on the simplicial mesh. Figure 5b shows the limiting is activated in a single element.

In contrast, Table 7 shows that the convergence rate without positivity detection degrades to $O(h^2)$ when $N = 3$ and degrades to $O(h)$ when $N = 4$ on the simplicial mesh. From Figure 6b, we observe the limiting is activated over the entire domain, even at regions where the density and pressure are nearly constant. It shows the sensitivity of Zalesak-type limiting with respect to the underlying sparse SBP operator, and the resulting limited solutions are overly dissipated. On the other hand, positivity detection eliminates the issue and recovers the high order convergence at smooth regions.

	$N = 1$		$N = 2$		$N = 3$		$N = 4$	
K_{1D}	L^1 error	Rate	L^1 error	Rate	L^1 error	Rate	L^1 error	Rate
2	3.241×10^0		1.579×10^0		2.516×10^0		1.512×10^0	
4	1.346×10^0	1.27	1.245×10^0	0.34	6.611×10^{-1}	1.93	5.415×10^{-1}	1.48
8	9.169×10^{-1}	0.55	3.254×10^{-1}	1.55	1.776×10^{-1}	1.90	8.944×10^{-2}	2.60
16	4.480×10^{-1}	1.03	7.862×10^{-2}	2.44	2.935×10^{-2}	2.89	7.943×10^{-3}	3.49
32	1.548×10^{-1}	1.53	1.030×10^{-2}	2.93	2.883×10^{-3}	3.66	2.341×10^{-4}	5.08

Table 6: Isentropic vortex, simplicial mesh - Elementwise (Zalesak-type) limiting with positivity detection

	$N = 1$		$N = 2$		$N = 3$		$N = 4$	
K	L^1 error	Rate	L^1 error	Rate	L^1 error	Rate	L^1 error	Rate
2	3.031×10^0		1.515×10^0		2.055×10^0		1.332×10^0	
4	1.256×10^0	1.27	1.198×10^0	0.34	7.907×10^{-1}	1.38	1.161×10^0	0.20
8	9.089×10^{-1}	0.47	5.029×10^{-1}	1.25	3.527×10^{-1}	1.16	9.058×10^{-1}	0.36
16	4.475×10^{-1}	1.02	1.304×10^{-1}	1.95	1.247×10^{-1}	1.50	6.115×10^{-1}	0.57
32	1.556×10^{-1}	1.52	4.072×10^{-2}	1.68	3.578×10^{-2}	1.80	3.915×10^{-1}	0.64

Table 7: Isentropic vortex, simplicial mesh - Elementwise (Zalesak-type) limiting without positivity detection

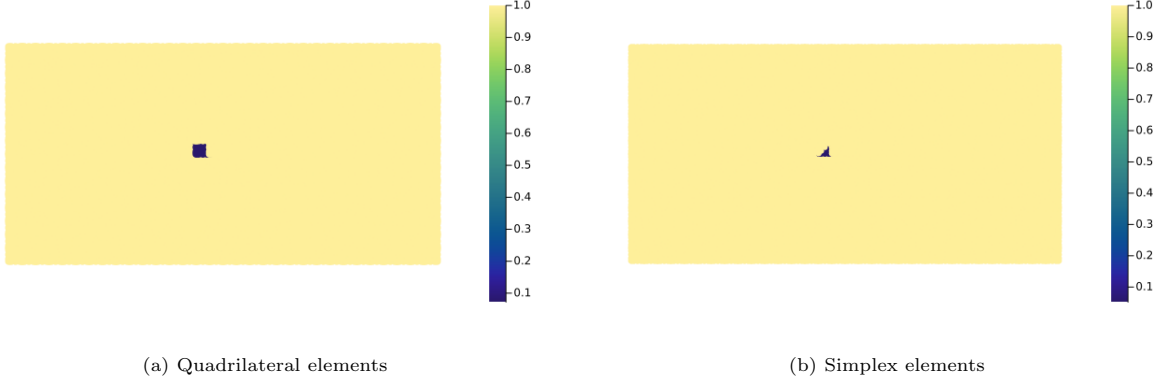


Figure 5: Isentropic vortex, limiting parameters, $N = 4$, $K_{1D} = 16$, $T = 0.25$, with positivity detection

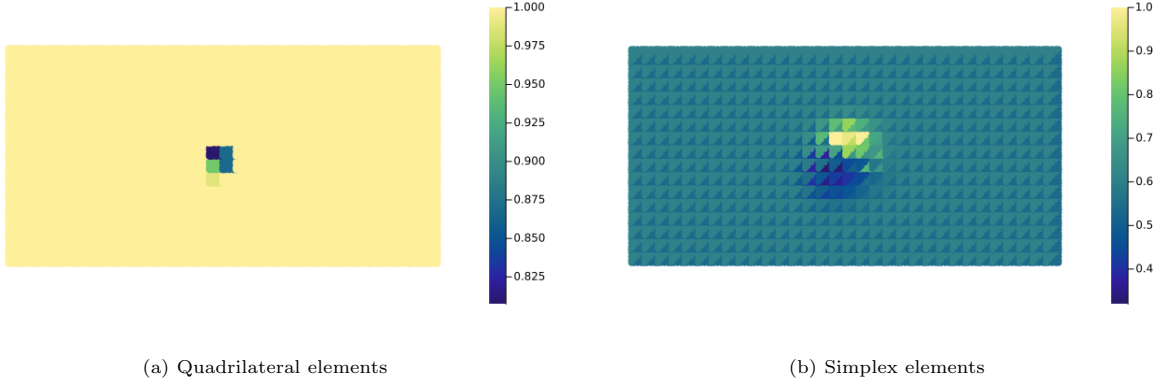


Figure 6: Isentropic vortex, limiting parameters, $N = 4$, $K_{1D} = 16$, $T = 1.0$, without positivity detection

8.2. Double Mach reflection

Finally we run the Double Mach Reflection [48] to verify the robustness of the proposed limiting strategies. The domain is $[0, 3.5] \times [0, 1]$, and the initial condition in primitive variables is

$$\mathbf{u}(x, y) = \begin{cases} \mathbf{u}_L, & \xi > 0 \\ \mathbf{u}_R, & \text{otherwise} \end{cases}, \quad \mathbf{u}_L = \begin{bmatrix} \rho_L \\ u_L \\ v_L \\ p_L \end{bmatrix} = \begin{bmatrix} 8.0 \\ 8.25 \cos(\pi/6) \\ -8.25 \sin(\pi/6) \\ 116.5 \end{bmatrix}, \quad \mathbf{u}_R = \begin{bmatrix} \rho_R \\ u_R \\ v_R \\ p_R \end{bmatrix} = \begin{bmatrix} 1.4 \\ 0.0 \\ 0.0 \\ 1.0 \end{bmatrix}, \quad (69)$$

where $\xi = y - \sqrt{3}x + \frac{\sqrt{3}}{6}$. We enforce reflective wall boundary conditions on $[\frac{1}{6}, 3.5] \times 0$ and assign $\mathbf{u}_L, \mathbf{u}_R$ as exterior values,

$$\mathbf{u}^+(x, y) = \begin{cases} \mathbf{u}_L, & \text{if } x \in [0, \frac{1}{6}] \times \{0\} \cup \{0\} \times [0, 1] \cup [0, s(t)] \times \{1\} \\ \mathbf{u}_R, & \text{if } x \in [s(t), 3.5] \times \{1\} \cup \{3.5\} \times [0, 1] \end{cases}, \quad s(t) = \frac{1 + \sqrt{3}/6}{\sqrt{3}} + \frac{10}{\cos(\pi/6)}t. \quad (70)$$

We discretize the domain by a uniform quadrilateral mesh with 875×250 elements, with polynomial degree $N = 3$. We run the simulation until $T = 0.2$ with both $Re = \infty$ (the compressible Euler equation) and $Re = 500$. We truncate the color range to $[1, 24]$ for clearer visualization, and we use 20 contours linearly spaced between the interval $[1, 24]$.

Finally, we note that proofs of positivity for the proposed limiting strategy do not account for non-periodic boundary conditions, and we observe that we do not necessarily preserve positivity at reflective wall boundaries. Therefore, for the compressible Navier-Stokes equations, we deactivate the positivity detector (48) on elements adjacent to reflective wall boundaries. This implies that limiting may be activated on such elements even if the high order solution on the element is positive, and in practice prevents simulations from encountering negative density or pressure near boundaries. Future work will address positivity-preserving limiting strategies in the presence of different boundary conditions.

In the following sections, we will present numerical results using Elementwise (Zalesak-type) limiting with positivity detection and Elementwise (Zhang-Shu type) limiting. Appendix A presents additional experiments using Elementwise (Zalesak-type) limiting without positivity detection.

8.2.1. Elementwise (Zalesak-type) limiting

We first run the simulations using Elementwise (Zalesak-type) limiting with positivity detection. In the presence of strong shocks, the simulations remain robust without any artificial viscosity or additional limiting. In addition, the simulations resolve fine scale vortices, showing the low numerical dissipation of the proposed elementwise (Zalesak-type) limiting strategy. When $Re = \infty$, in Figure 7, we observe numerical artifacts near shocks which perturb the vortices. The numerical oscillations can be suppressed with additional shock capturing or limiting. On the other hand, when $Re = 500$, the physical dissipation is enough to suppress the numerical oscillations, and the fine scale vortices are still resolved as shown in Figure 10.

8.2.2. Elementwise (Zhang-Shu type) limiting

Finally, results using Elementwise (Zhang-Shu type) limiting are shown in Figure 8. We observe similar results compared to the solutions using Elementwise (Zalesak-type) limiting with positivity detection in Figure 7. The simulations remain robust, resolve fine scale features, and produce spurious oscillations near shocks. However, one of the main differences between two approaches is that Elementwise (Zhang-Shu type) limiting takes a significantly larger number of timesteps to finish the simulation, as shown in Figure 9.

The average timestep sizes of the simulations using Elementwise (Zalesak-type) and (Zhang-Shu type) limiting are 1.15×10^{-6} and 4.41×10^{-7} , respectively. Since Elementwise (Zalesak-type) limiting is a more pessimistic limiting strategy, the maximum wavespeed λ_{\max} defined in (28) over all pairs of nodes in the domain is smaller, resulting in a slightly more dissipative limiting. This appears to be sufficient to avoid artificial decreases in timestep sizes due to near-zero density and pressure.

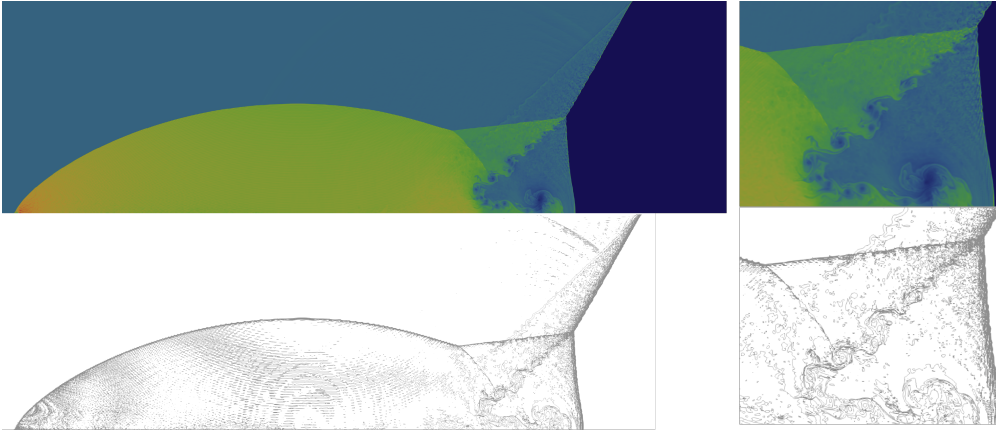


Figure 7: Double Mach Reflection, $Re = \infty$, Elementwise (Zalesak-type) limiting with positivity detection

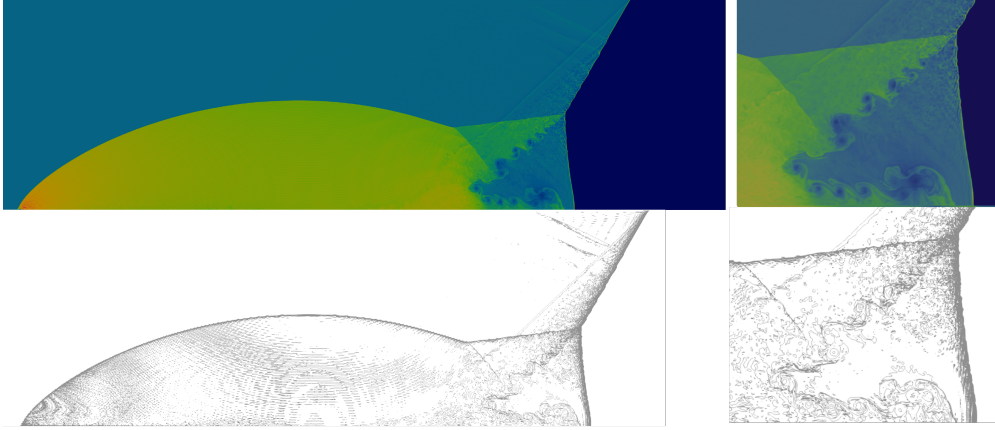


Figure 8: Double Mach Reflection, $Re = \infty$, Elementwise (Zhang-Shu type) limiting

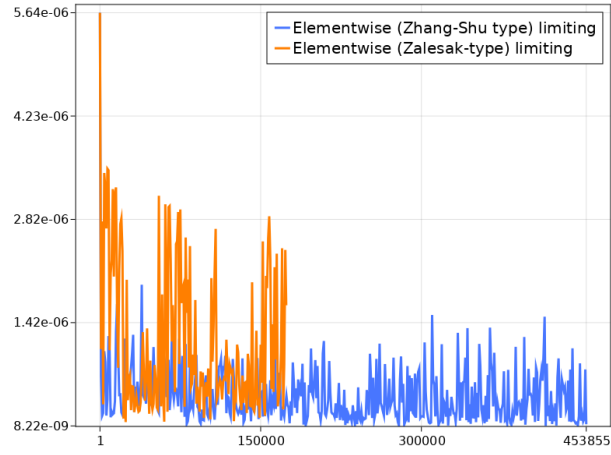


Figure 9: Double Mach Reflection - timestep history

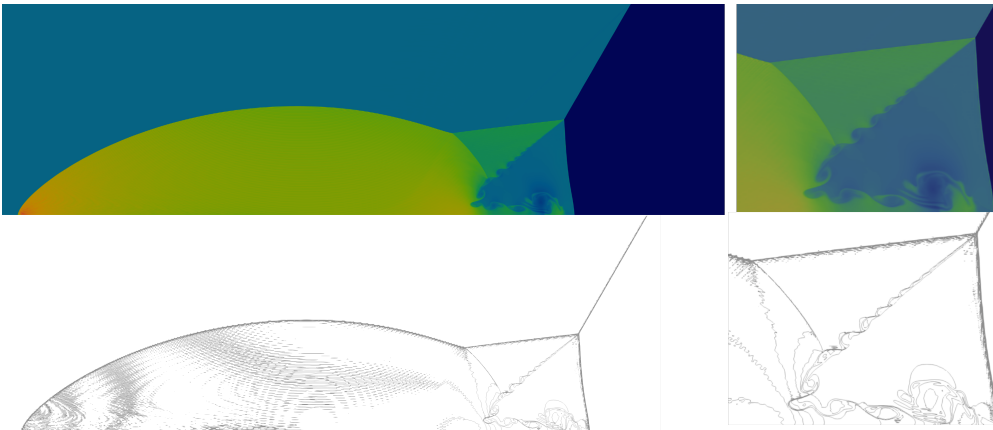


Figure 10: Double Mach Reflection, $Re = 500$, Elementwise (Zalesak-type) limiting with positivity detection

9. Conclusion

In this paper, we present a positivity limiting strategy based on algebraic flux corrections. We construct a low order positivity preserving discretization for the compressible Euler and Navier-Stokes equations using the graph viscosity terms. The entropy stable discretizations are then blended with the positivity preserving discretization by convex limiting. The proposed limiting solutions preserve positivity and satisfy discrete entropy balances for both equations.

Acknowledgement

Yimin Lin and Jesse Chan gratefully acknowledge support from National Science Foundation under awards DMS-1719818 and DMS-CAREER-1943186. This work used the Extreme Science and Engineering Discovery Environment (XSEDE) Expanse at the San Diego Supercomputer Center through allocation TG-MTH200014 [49]. The work of IT was partially supported by the U.S. Department of Energy, Office of Science, Office of Advanced Scientific Computing Research, Applied Mathematics Program and by the U.S. Department of Energy, Office of Science, Office of Advanced Scientific Computing Research and Office of Fusion Energy Sciences, Scientific Discovery through Advanced Computing (SciDAC) program. This manuscript has been authored by National Technology & Engineering Solutions of Sandia, LLC., under contract DE-NA0003525 with the U.S. Department of Energy/National Nuclear Security Administration. The United States Government retains and the publisher, by accepting the article for publication, acknowledges that the United States Government retains a non-exclusive, paid-up, irrevocable, world-wide license to publish or reproduce the published form of this manuscript, or allow others to do so, for United States Government purposes.

A. Additional numerical experiments

In this section, we present additional double Mach reflection experiments using other limiting strategies. We use the exact same configurations as in Section 8.2. Figure 11 and 12 shows the Nodal limited solutions when $Re = \infty$ and 500. Although the simulations remain robust, we observe spurious oscillations near vortices. The oscillations may correlate with the loss of discrete entropy, and they require further investigations.

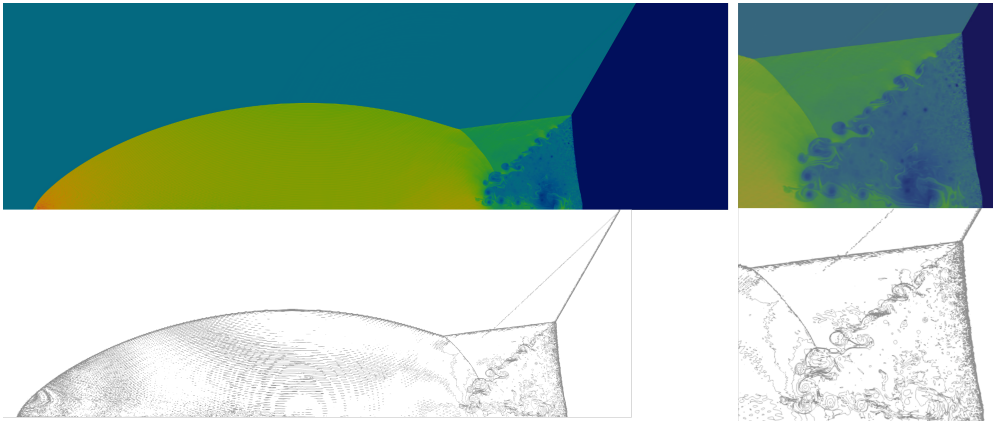


Figure 11: Double Mach Reflection, $Re = \infty, \rho$, Nodal limiting strategy

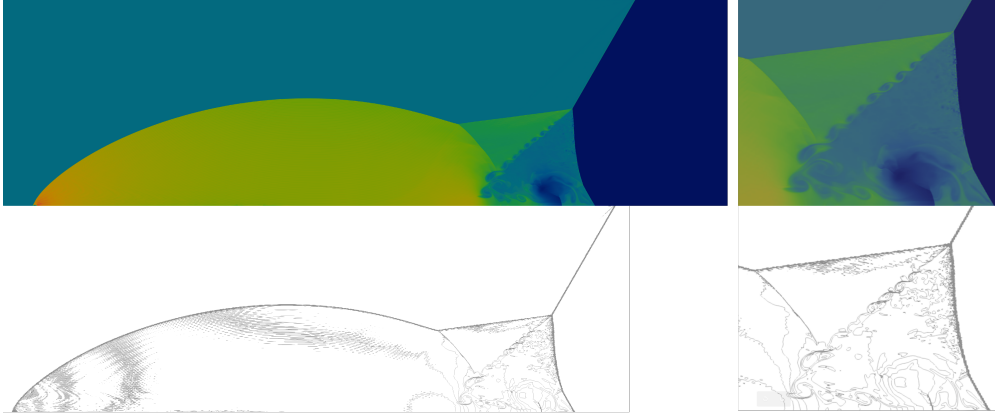


Figure 12: Double Mach Reflection, $Re = 500, \rho$, Nodal limiting strategy

We then run the simulations with Elementwise (Zalesak-type) limiting without positivity detection. The simulations remain robust and resolve fine scale vortices. Compared to the results in Figure 7 and 10, Elementwise (Zalesak-type) limiting without positivity detection introduces extra numerical dissipation into the discretizations. As a result, the numerical oscillations near shocks are absent. However, this strategy negatively impacts high order accuracy, and may still not be sufficient to ensure that numerical oscillations disappear in all test cases.

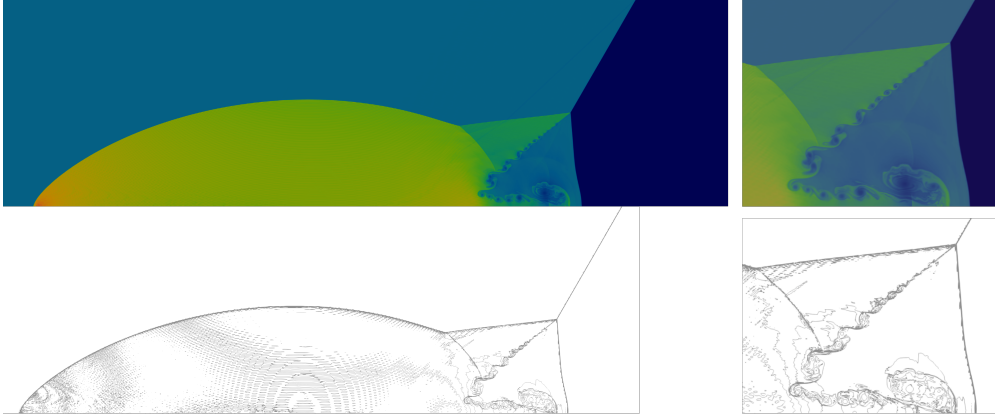


Figure 13: Double Mach Reflection, $Re = \infty$, Elementwise (Zalesak-type) limiting without positivity detection

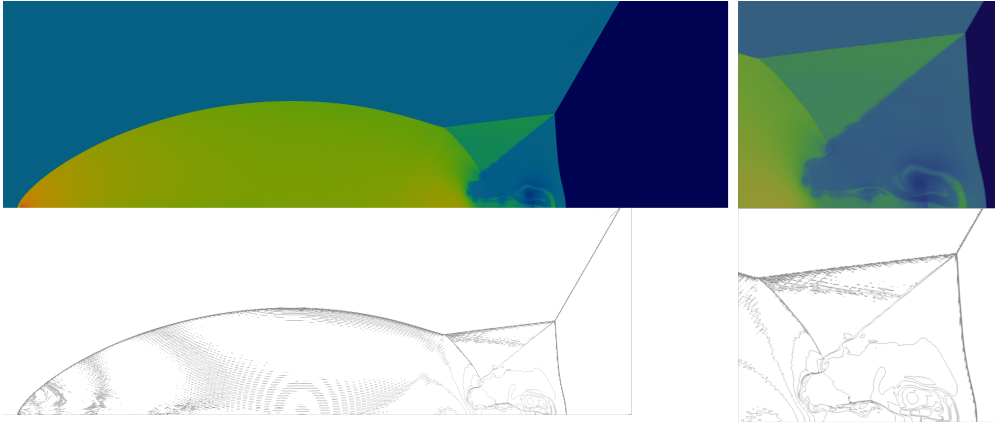


Figure 14: Double Mach Reflection, $Re = 500$, Elementwise (Zalesak-type) limiting without positivity detection

References

- [1] J. Slotnick, A. K. PM, J. Alonso, D. Darmofal, W. Gropp, E. Lurie, D. Mavriplis, CFD vision 2030 study: a path to revolutionary computational aerosciences (2013).
- [2] Z. J. Wang, K. Fidkowski, R. Abgrall, F. Bassi, D. Caraeni, A. Cary, H. Deconinck, R. Hartmann, K. Hillewaert, H. T. Huynh, et al., High-order CFD methods: current status and perspective, *International Journal for Numerical Methods in Fluids* 72 (8) (2013) 811–845.
- [3] J. S. Hesthaven, T. Warburton, *Nodal discontinuous Galerkin methods: algorithms, analysis, and applications*, Springer Science & Business Media, 2007.
- [4] J. Chan, On discretely entropy conservative and entropy stable discontinuous Galerkin methods, *Journal of Computational Physics* 362 (2018) 346–374.
- [5] J. Chan, Skew-symmetric entropy stable modal discontinuous Galerkin formulations, *Journal of Scientific Computing* 81 (1) (2019) 459–485.
- [6] J. Chan, Y. Lin, T. Warburton, Entropy stable modal discontinuous Galerkin schemes and wall boundary conditions for the compressible Navier-Stokes equations, *Journal of Computational Physics* 448 (2022) 110723.
- [7] M. H. Carpenter, T. C. Fisher, E. J. Nielsen, S. H. Frankel, Entropy stable spectral collocation schemes for the Navier-Stokes equations: Discontinuous interfaces, *SIAM Journal on Scientific Computing* 36 (5) (2014) B835–B867.
- [8] G. J. Gassner, A skew-symmetric discontinuous Galerkin spectral element discretization and its relation to SBP-SAT finite difference methods, *SIAM Journal on Scientific Computing* 35 (3) (2013) A1233–A1253.
- [9] G. J. Gassner, A. R. Winters, D. A. Kopriva, Split form nodal discontinuous Galerkin schemes with summation-by-parts property for the compressible Euler equations, *Journal of Computational Physics* 327 (2016) 39–66.
- [10] T. Chen, C.-W. Shu, Entropy stable high order discontinuous Galerkin methods with suitable quadrature rules for hyperbolic conservation laws, *Journal of Computational Physics* 345 (2017) 427–461.
- [11] G. J. Gassner, M. Svärd, F. J. Hindenlang, Stability issues of entropy-stable and/or split-form high-order schemes, *arXiv preprint arXiv:2007.09026* (2020).
- [12] L. Krivodonova, Limiters for high-order discontinuous Galerkin methods, *Journal of Computational Physics* 226 (1) (2007) 879–896.
- [13] P.-O. Persson, J. Peraire, Sub-cell shock capturing for discontinuous Galerkin methods, in: *44th AIAA Aerospace Sciences Meeting and Exhibit*, 2006, p. 112.
- [14] X. Zhang, C.-W. Shu, On maximum-principle-satisfying high order schemes for scalar conservation laws, *Journal of Computational Physics* 229 (9) (2010) 3091–3120.
- [15] X. Zhang, C.-W. Shu, Maximum-principle-satisfying and positivity-preserving high-order schemes for conservation laws: survey and new developments, *Proceedings of the Royal Society A: Mathematical, Physical and Engineering Sciences* 467 (2134) (2011) 2752–2776.
- [16] X. Zhang, On positivity-preserving high order discontinuous Galerkin schemes for compressible Navier–Stokes equations, *Journal of Computational Physics* 328 (2017) 301–343.
- [17] X. Zhang, C.-W. Shu, On positivity-preserving high order discontinuous Galerkin schemes for compressible Euler equations on rectangular meshes, *Journal of Computational Physics* 229 (23) (2010) 8918–8934.
- [18] D. Kuzmin, M. Q. de Luna, Subcell flux limiting for high-order Bernstein finite element discretizations of scalar hyperbolic conservation laws, *Journal of Computational Physics* 411 (2020) 109411.
- [19] J.-L. Guermond, B. Popov, Invariant domains and first-order continuous finite element approximation for hyperbolic systems, *SIAM Journal on Numerical Analysis* 54 (4) (2016) 2466–2489.
- [20] J.-L. Guermond, M. Nazarov, B. Popov, I. Tomas, Second-order invariant domain preserving approximation of the Euler equations using convex limiting, *SIAM Journal on Scientific Computing* 40 (5) (2018) A3211–A3239.
- [21] J.-L. Guermond, B. Popov, I. Tomas, Invariant domain preserving discretization-independent schemes and convex limiting for hyperbolic systems, *Computer Methods in Applied Mechanics and Engineering* 347 (2019) 143–175.
- [22] J.-L. Guermond, M. Maier, B. Popov, I. Tomas, Second-order invariant domain preserving approximation of the compressible Navier–Stokes equations, *Computer Methods in Applied Mechanics and Engineering* 375 (2021) 113608.
- [23] M. Dumbser, O. Zanotti, R. Loubère, S. Diot, A posteriori subcell limiting of the discontinuous Galerkin finite element method for hyperbolic conservation laws, *Journal of Computational Physics* 278 (2014) 47–75.
- [24] M. Sonntag, C.-D. Munz, Shock capturing for discontinuous Galerkin methods using finite volume subcells, in: *Finite Volumes for Complex Applications VII-Elliptic, Parabolic and Hyperbolic Problems*, Springer, 2014, pp. 945–953.
- [25] F. Vilar, A posteriori correction of high-order discontinuous Galerkin scheme through subcell finite volume formulation and flux reconstruction, *Journal of Computational Physics* 387 (2019) 245–279.
- [26] A. M. Rueda-Ramírez, G. J. Gassner, A Subcell Finite Volume Positivity-Preserving Limiter for DGSEM Discretizations of the Euler Equations, *arXiv preprint arXiv:2102.06017* (2021).
- [27] S. Hennemann, A. M. Rueda-Ramírez, F. J. Hindenlang, G. J. Gassner, A provably entropy stable subcell shock capturing approach for high order split form DG for the compressible Euler equations, *Journal of Computational Physics* 426 (2021) 109935.
- [28] J. Upperman, N. K. Yamaleev, First-order positivity-preserving entropy stable spectral collocation scheme for the 3-D compressible Navier-Stokes equations, *arXiv preprint arXiv:2111.03239* (2021).
- [29] W. Pazner, Sparse invariant domain preserving discontinuous Galerkin methods with subcell convex limiting, *Computer Methods in Applied Mechanics and Engineering* 382 (2021) 113876.
- [30] J. Chan, L. Demkowicz, R. Moser, A DPG method for steady viscous compressible flow, *Computers & Fluids* 98 (2014) 69–90.

- [31] T. J. Hughes, L. Franca, M. Mallet, A new finite element formulation for computational fluid dynamics: I. Symmetric forms of the compressible Euler and Navier-Stokes equations and the second law of thermodynamics, *Computer Methods in Applied Mechanics and Engineering* 54 (2) (1986) 223–234.
- [32] X. Wu, E. J. Kubatko, J. Chan, High-order entropy stable discontinuous Galerkin methods for the shallow water equations: curved triangular meshes and GPU acceleration, *Computers & Mathematics with Applications* 82 (2021) 179–199.
- [33] J. Crean, J. E. Hicken, D. C. D. R. Fernández, D. W. Zingg, M. H. Carpenter, High-order, entropy-stable discretizations of the Euler equations for complex geometries, in: *23rd AIAA Computational Fluid Dynamics Conference*. American Institute of Aeronautics and Astronautics, 2017.
- [34] D. C. D. R. Fernández, J. E. Hicken, D. W. Zingg, Review of summation-by-parts operators with simultaneous approximation terms for the numerical solution of partial differential equations, *Computers & Fluids* 95 (2014) 171–196.
- [35] X. Wu, N. Trask, J. Chan, Entropy stable discontinuous Galerkin methods for the shallow water equations with subcell positivity preservation (2021). [arXiv:2112.07749](https://arxiv.org/abs/2112.07749).
- [36] N. Trask, P. Bochev, M. Perego, A conservative, consistent, and scalable meshfree mimetic method, *Journal of Computational Physics* 409 (2020) 109187.
- [37] E. Tadmor, The numerical viscosity of entropy stable schemes for systems of conservation laws. I, *Mathematics of Computation* 49 (179) (1987) 91–103.
- [38] E. Tadmor, Entropy stability theory for difference approximations of nonlinear conservation laws and related time-dependent problems, *Acta Numerica* 12 (1) (2003) 451–512.
- [39] P. Chandrashekar, Kinetic energy preserving and entropy stable finite volume schemes for compressible Euler and Navier-Stokes equations, *Communications in Computational Physics* 14 (5) (2013) 1252–1286.
- [40] G. J. Gassner, A. R. Winters, F. J. Hindenlang, D. A. Kopriva, The BR1 scheme is stable for the compressible Navier-Stokes equations, *Journal of Scientific Computing* 77 (1) (2018) 154–200.
- [41] J. P. Boris, D. L. Book, Flux-corrected transport. I. SHASTA, a fluid transport algorithm that works, *Journal of computational physics* 11 (1) (1973) 38–69.
- [42] Y. Liu, C.-W. Shu, M. Zhang, Entropy stable high order discontinuous Galerkin methods for ideal compressible MHD on structured meshes, *Journal of Computational Physics* 354 (2018) 163–178.
- [43] F. Renac, Entropy stable DGSEM for nonlinear hyperbolic systems in nonconservative form with application to two-phase flows, *Journal of Computational Physics* 382 (2019) 1–26.
- [44] A. Harten, J. M. Hyman, P. D. Lax, B. Keyfitz, On finite-difference approximations and entropy conditions for shocks, *Communications on pure and applied mathematics* 29 (3) (1976) 297–322.
- [45] S. T. Zalesak, Fully multidimensional flux-corrected transport algorithms for fluids, *Journal of computational physics* 31 (3) (1979) 335–362.
- [46] C.-W. Shu, S. Osher, Efficient implementation of essentially non-oscillatory shock-capturing schemes, *Journal of computational physics* 77 (2) (1988) 439–471.
- [47] F. Ismail, P. L. Roe, Affordable, entropy-consistent Euler flux functions II: Entropy production at shocks, *Journal of Computational Physics* 228 (15) (2009) 5410–5436.
- [48] P. Woodward, P. Colella, The numerical simulation of two-dimensional fluid flow with strong shocks, *Journal of computational physics* 54 (1) (1984) 115–173.
- [49] J. Towns, T. Cockerill, M. Dahan, I. Foster, K. Gaither, A. Grimshaw, V. Hazlewood, S. Lathrop, D. Lifka, G. D. Peterson, R. Roskies, J. Scott, N. Wilkins-Diehr, XSEDE: Accelerating Scientific Discovery, *Computing in Science and Engineering* 16 (05) (2014) 62–74.